Heriot-Watt University

PhD Thesis

Lessons in Solvent Design for Low Dimensional Systems Using the Corresponding Distances Method

Author:
Adam Hardy

Supervisors:
Dr. Henry Bock
Dr. Robin Westacott

A thesis submitted in fulfilment of the requirements for the degree of Doctor of Philosophy

in the

School of Engineering and Physical Sciences

May 2018

"The chances of finding out what really is going on are so absurdly remote that the only thing to do is to say hang the sense of it and keep yourself occupied."

Slartibartfast, in *The Hitchhikers Guide to the Galaxy*, Douglas Adams.

Abstract

Low dimensional materials such as graphene and carbon nanotubes have frequently been hailed as breakthrough materials, however, despite much experimental and theoretical research these two materials have struggled to make their way into commercial products. One of the key difficulties is in the processing of the raw material; separating the aggregated nano-material into a dispersion of individualised particles. Current techniques require significant energy input and produce low quality dispersions in terms of yield, overall loading and quality of the nano-particles.

Simulation is a convenient way to study this problem, via calculation of the potential of mean force (PMF) to obtain a free energy profile of the dispersion process. Current simulation techniques are resource heavy, slow and have difficulty maintaining thermodynamic consistency. We will present the corresponding distance method (CDM)as an improved method to calculate PMFs.

PMF calculations from the CDM will be used in combination with detailed structural analysis and comparison to experimental results to investigate solvent molecules, the mechanism of dispersion, and derive design rules to serve as guidelines for future work.

Acknowledgements

First I would like to thank my supervisors: Dr Henry Bock and Dr Robin Westacott. Henry for his time, contributions and guidance across four years, and Robin for picking me up and seeing me through the last four months. I'd also like to give my gratitude to Dr. Alex Bell for his support and guidance through some difficult times.

To all the members of Heriot Watt University Boat Club who have been an extended family for me, particularly Graeme for his unwavering dedication to the club.

To everyone in the office: Jane, Dawn, Fiona and Abou.

Lastly, my mum and dad for their gentle nagging in the final few weeks; my girlfriend Shona for her support and all the rest of my friends and family, especially those who are no longer with us.

ACADEMIC REGISTRY

Research Thesis Submission

Name*:*			
School:			
Version: *(i.e. First, Resubmission, Final)*		Degree Sought:	

Declaration

In accordance with the appropriate regulations I hereby submit my thesis and I declare that:

1) the thesis embodies the results of my own work and has been composed by myself
2) where appropriate, I have made acknowledgement of the work of others and have made reference to work carried out in collaboration with other persons
3) the thesis is the correct version of the thesis for submission and is the same version as any electronic versions submitted*.
4) my thesis for the award referred to, deposited in the Heriot-Watt University Library, should be made available for loan or photocopying and be available via the Institutional Repository, subject to such conditions as the Librarian may require
5) I understand that as a student of the University I am required to abide by the Regulations of the University and to conform to its discipline.
6) I confirm that the thesis has been verified against plagiarism via an approved plagiarism detection application e.g. Turnitin.

* *Please note that it is the responsibility of the candidate to ensure that the correct version of the thesis is submitted.*

Signature of Candidate*:*		Date:	

Submission

Submitted By *(name in capitals):*	
Signature of Individual Submitting:	
Date Submitted:	

For Completion in the Student Service Centre (SSC)

Received in the SSC by *(name in capitals):*			
Method of Submission *(Handed in to SSC; posted through internal/external mail):*			
*E-thesis Submitted (**mandatory for final theses)***			
Signature:		Date:	

Please note this form should be bound into the submitted thesis.

Contents

Abbreviations

CDM	**C**orrespnding **D**istance **M**ethod
PMF	**P**otential of **M**ean **F**orce
ttPMF	**T**ube - **T**ube **PMF**
ssPMF	**S**heet - **S**heet **PMF**
smPMF	**S**olvent **M**ediated **PMF**
CNT	**C**arbon **N**ano**t**ube

Symbols

$w(d)$	PMF	kT nm^{-1} **or** kJ mol^{-1} nm^{-1} (carbon nanotubes) kT nm^{-2} (graphene)
w_{agg}	aggregate stability	kT nm^{-1} **or** kJ mol^{-1} nm^{-1} (carbon nanotubes) kT nm^{-2} (graphene)
w_{reagg}	reaggregation barrier height	kT nm^{-1} **or** kJ mol^{-1} nm^{-1} (carbon nanotubes) kT nm^{-2} (graphene)
w_{disp}	dispersion barrier height	kT nm^{-1} **or** kJ mol^{-1} nm^{-1} (carbon nanotubes) kT nm^{-2} (graphene)
$F(d)$	Mean Force	kT nm^{-2} **or** kJ mol^{-1} nm^{-2} (carbon nanotubes) kT nm^{-3} (graphene)
d	material surface-surface distance	nm
r	cut-off	nm
R	distance	nm
ϵ	Lennard-Jones distance parameter	kJ mol^{-1}
σ	Lennard-Jones length parameter	nm

For Richard (1948 - 2015) . . .

Chapter 1

Introduction

1.1 Low Dimensional Materials

Low-dimensional materials are so called because they are confined in one or more dimensions. They can be split into three categories (Figure 1.1):

- 0-dimensional: confined in all 3 dimensions e.g. a gold nano-particle.
- 1-dimensional: one long dimension e.g. a carbon nanotube.
- 2-dimensional: two long dimensions e.g. a graphene sheet

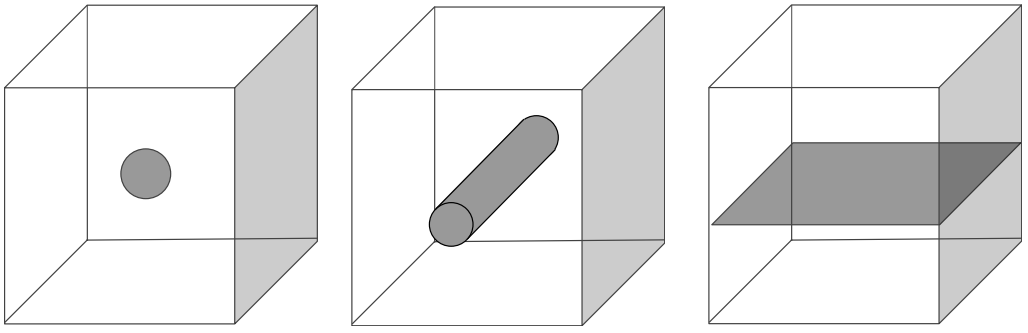

(A) 0-D material (B) 1-D material (C) 2-D material

FIGURE 1.1: The three types of low-dimensional materials.

0-D materials can be processed using conventional liquid phase processing techniques and used in large scale industrial processes [1]. 1-D and 2-D materials, however, present a unique problem. Even if only small attractive forces exist between adjacent particles, because these materials posses (at least) one long dimension, these forces become extremely large. Aggregation is very favourable and dispersing them can be very difficult. This dispersion problem is the focus of this thesis.

1.2 Theoretical Techniques

1.2.1 Modelling

Molecular modelling is a valuable tool for investigating these sorts of problems; we can gather far more information on a system than is available in experiment. Not only can we measure forces and energies, we have the precise position of every atom so can observe detailed structural phenomena that are difficult or impossible to observe in experiment.

There are several techniques available to study atomistic systems. Quantum mechanical (QM) based methods (such as density functional theory or Hartree-Fock) are very computationally demanding and impractical for the sizes required of our systems. Even a hybrid method using only QM at the nano-material's surface would still be far too slow.

Atomistic simulations based in classical physics offer a satisfactory compromise between speed and accuracy. Here there are two main candidates: Monte Carlo and molecular dynamics (MD). Monte Carlo simulation, named for the famous casinos of Monaco, is a method based in equilibrium statistical mechanics, generating possible states based on Boltzmann probabilities to sample a system. We will use molecular dynamics simulation which, rather than sampling possible states, attempts to recreate the dynamics of a system by modelling atoms using classical mechanics and solving Newton's equations of motion to calculate trajectories and produce the next frame of the simulation.

MD offers excellent opportunities for parallelisation and many of the common MD codes are highly scalable across multi-CPU and multi-GPU computers, meaning even very large simulations can be completed very quickly provided enough CPU or GPU cores are available.

1.2.2 The Corresponding Distances Method

Experimentally, dispersion is easy to measure, we simply need to measure the amount of dispersed material. In simulation we commonly rely on the potential of mean force (PMF), $w(d)$. The PMF provides the free energy dependence of the system on the distance between two particles, d. Current theoretical methods to calculate the PMF are computationally slow, suffer from problems with thermodynamic consistency and integration, and (due to the large number of simulations typically required) are administratively difficult to manage. The difficulty in performing PMF calculations currently limits the scope of investigations.

Core to this work is the corresponding distances method (CDM), which improves on current methods to calculate PMFs. This was first demonstrated in coarse grained dissipative particle

dynamics simulations [2] and we will demonstrate its effectiveness in atomistic molecular dynamics.

Current techniques rely on performing many un-connected simulations of a pair of parallel tubes at varying tube-tube distance, d. In the CDM the tubes are placed in the simulation box at a small angle, and this way all d are present in the system at the same time. Mean force,$F(d)$, is measured at intervals down each tube, and then distance, d, to the opposite tube is calculated by measuring the distance to the first solvent layer, and then the distance from there to the opposite tube (as shown for carbon nanotubes in Figure 1.2). This gives us the entire PMF in one simulation.

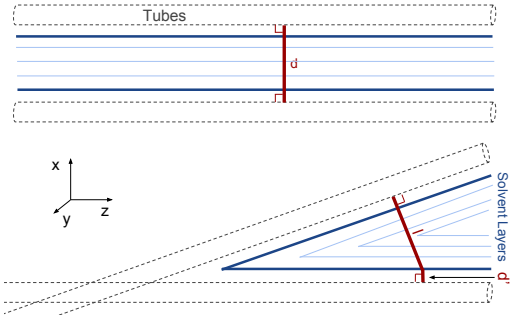

FIGURE 1.2: Schematic comparison of a parallel tube system (top) and CDM system (bottom). The dashed lines represent the nanotubes and the blue solid lines represent the solvent layers that form between tubes. The red lines show how the tube-tube distance, d, is calculated in each case.

There are 3 key advantages of the CDM:

1. Speed and efficiency: the amount of bulk solvent is reduced compared to the equivalent in parallel simulations leading to faster simulation times.

2. Thermodynamic consistency: each data point is guaranteed to be in the same thermodynamic state. This is tricky to achieve across independent simulations.

3. Reduced administrative overhead: one need only set up, run and collect data from one simulation. Even using automation to manage the multiple parallel simulations, this results in a significant reduction in operator time.

Full details of the configuration and methods used with the CDM can be found in Chapter 3.

1.3 Objectives

1. Demonstrate a new theoretical technique to study the dispersion of low dimension materials.

2. Demonstrate the concept on multiple materials by comparison to available experimental data.

3. Use the new technique to study a range of systems.

4. Draw meaningful conclusions from these results to guide further experimental and theoretical work.

1.4 Thesis Outline

In Chapter 3 we introduce the problem and how the the corresponding distance method can help solve it. We compare the CDM to a conventional technique to calculate the PMF for carbon nanotubes dispersed in $CBrCl_3$ and attempt to answer why $CBrCl_3$ is a poor carbon nanotube solvent in experiment, despite being predicted to be a good one according to solubility parameters [3].

We then take advantage of the CDM to expand our study in Chapter 4, to ten solvent molecules. These ten molecules are a selection of good and bad CNT solvents as tested in experiment by Bergin et al. [3]. We see excellent agreement between our simulations and experiment and are able to draw important conclusions on the mechanism of CNT dispersion and how to progress in CNT solvent design.

Chapter 5 is devoted to demonstrating the CDM with a 2-D material, graphene. We again use $CBrCl_3$ as our test case but also take a look at water. Graphene and CNTs are chemically almost identical, they differ only in macro-structure, so we can also take a look at the effect of nano-material shape on solvent performance.

In Chapter 6 we perform a simplified chemical optimization in the search for a CNT solvent and then apply the lessons learnt to propose improved solvent systems.

Finally, in Chapter 7, we present our concluding remarks and suggest possible directions for future work.

Bibliography

[1] Hellgren, A.-C., Weissenborn, P., and Holmberg, K. (1999) Surfactants in water-borne paints. *Prog. Org. Coat. 35*, 79–87.

[2] Müter, D., Angelikopoulos, P., and Bock, H. (2012) Angular Dependence of Surfactant-Mediated Forces Between Carbon Nanotubes. *The Journal of Physical Chemistry B 116*, 14869–14875.

[3] Bergin, S. D., Sun, Z., Rickard, D., Streich, P. V., Hamilton, J. P., and Coleman, J. N. (2009) Multicomponent Solubility Parameters for Single-Walled Carbon Nanotube-Solvent Mixtures. *ACS Nano 3*, 2340–2350.

Chapter 2

Background to the Research

2.1 Carbon Nanotubes and Graphene

The two materials we will focus on most in this thesis are carbon nanotubes (1-D, Figure 2.1a), and graphene (2-D, Figure 2.1b). Because of their unique structures these materials exhibit several desirable properties which make them useful in a wide range of applications: ultra-strong, ultra-light materials [1]; transistors [2]; electrodes [3] and molecular sieves [4] amongst others.

While graphene has only one possible structure, carbon nanotubes have many. CNTs can be single or multi-walled; a single walled carbon nanotube can be thought of as a single rolled layer of graphite and is the kind shown in Figure 2.1a. Multi-walled tubes contain several concentric rings of graphite. CNTs can also differ in their chirality. This is the angle at which the graphene sheet has been rolled to form a tube. Chiralty is measured by two indexes n and m which are the two vectors on the graphene sheet, usually given in the form: (n, m). These two numbers together determine: the angle at which the graphene sheets meets itself when rolled into a tube, and the diameter of the formed tube. Tube chirality and number of walls can significantly affect the nanotube's physical properties, particular its electrical properties (determining whether a tube is metallic or semi-conducting for example). In this work we consider only one type of tube: (10,10) singled walled CNTs. This type of tube is particularly convenient for us, as it means the carbon atoms are regularly spaced down the length of the nanotube. The diameter of these tubes (1.36 nm) is similar to that used in the experimental work we will refer to as a comparison for our simulations.[5]

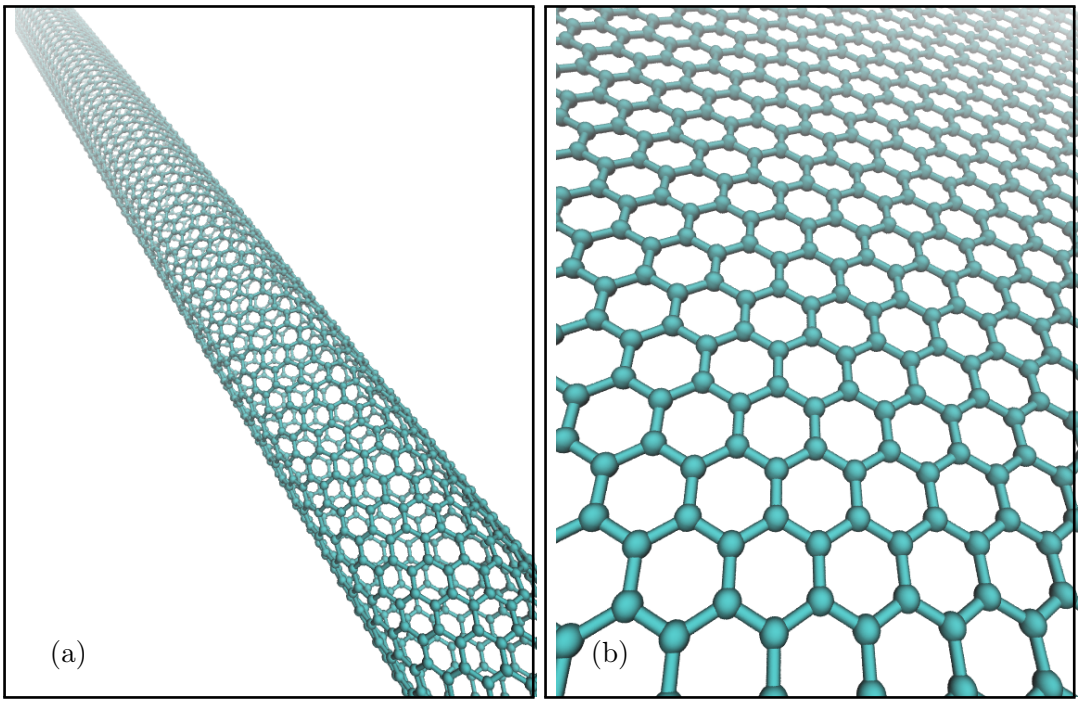

FIGURE 2.1: Visualisations of a carbon nanotube (left, a) and a graphene sheet (right, b). Graphene is a single layer of hexagonally arranged carbon atoms. Each carbon atom is sp^2 hybridized and covalently bonded to three others, similar to benzene. The covalent bond network and highly mobile electrons on the graphene surface are responsible for the material's mechanical, thermal and electronic properties. A carbon nanotube is essentially a rolled up graphene sheet and such shows very similar physical properties.

2.2 The Dispersion Problem

As manufactured, carbon nanotubes are in an aggregated (bundled) state but require individualisation to before we can make use of their unique properties. For example, metallic type CNTs could be introduced to an electrically insulating polymer to create a conducting composite. Any additional tubes in a bundle beyond the first are wasted and large bundles will cause the composite material to turn dark black.

Unfortunately individualisation remains difficult. The potential minimum in a vacuum between a pair of aggregated (10,10) nanotubes over the length of a unit cell ($0.37nm$) is $-16.5\ kT$. A small amount of energy input combined with thermal fluctuations would be sufficient to overcome this. The problem comes because of the geometry of 1D and 2D materials; this energy is summed over the entire length of the material. Extend the length of the tube above to 1nm and the the interaction energy increases to $-45\ kT$ which is now difficult to achieve using just thermal or mechanical means.

However, tubes need to be much longer to be useful; micrometer long tubes are not unusual and up to centimetres long [6] is possible. The energy required to separate the two tubes can

become colossal; thousands of kT. In the case of a two-dimensional material, the aggregate energy increases not just with length, but also width.

Liquid phase processing is likely the only technique that will adequately separate bundled CNTs without causing extensive damage to the tubes; it is also an extremely common and easy technique at industrial scales. Ideally, we would have a solvent that creates high quality dispersions of individual tubes in commercially feasible quantities in a low energy process.

Current-processes almost exclusively require ultra-sonication (which is both difficult to scale and energy intensive) and, regardless of the type of dispersant used, produce low quality dispersions with low tube concentrations, typically in the range O(1)mg mL^{-1}[5, 7–12].

2.3 Experiment

2.3.1 CNT Solvents

Aqueous surfactant solutions are the most common applied dispersion method, typically using molecules such as sodium dodecyl sulfate (SDS) [8], sodium dodecyl benzene sulfonate (SDBS) [8, 9] or triton X-100 [13], combined with ultra-sonication and ultra-centrifugation. The amphiphilic surfactant molecules are able to absorb on the CNT surface with their hydrophobic parts, leaving the hydrophilic head groups exposed, effectively rendering the whole surface hydrophilic. In an aqueous solution these hydrophilic surfaces repel each other and prevent the nano-material from aggregating.

While some surfactant systems have been shown to stabilise CNT suspensions well, they do not seem to be effective at aiding the dispersion process and some computer simulations suggest that surfactants may actually act to stabilise CNT aggregates [14, 15] and potentially hinder exfoliation. Surfactants also leave a difficult-to-remove residue on the dispersed material which can adversely affect the material properties [16]. For these reasons, we concentrate our research on pure solvent-systems which avoid the above problems.

Current pure-solvent systems share the use of ultra-sonication and ultra-centrifugation required by surfactant systems. N-methyl-2-pyrrolidone (NMP) is the most widely used pure solvent for this application [11]. An extensive experimental study by Bergin *et al.* [5] measured CNT dispersion in a large number of candidate CNT solvents. Of the dozens tested, all bar one obtained CNT loadings (often significantly) less than 1 mg mL^{-1}. The stand-out from this study was N-cyclohexyl-2-pyrrolidone (CHP), dispersing 1 mg mL^{-1}, over 5 times the next best solvent. The researchers then attempted to use solubility parameters to predict solvent performance, meeting with some success (see Section 2.4).

2.3.2 Graphene Solvents

Dispersion techniques are very similar between the two materials, sharing similar mechanical exfoliation methods (sonication or high-shear mixing [17, 18]), combined with a liquid-phase dispersant. Several classes of dispersant have been investigated; including organic solvents [19], block copolymers [20] and aqueous solutions containing surfactants [21]. Dispersions of graphene also suffer from low loadings and poor quality of the dispersed particles. A study of over 40 graphene pure-solvent systems found a maximum loading of just 8 μg mL^{-1}, orders of magnitude worse than the equivalent study of CNT solvents, though the authors of the study admit that they did not have an optimized dispersion protocol for graphene.

While graphene and CNTs share many similarities, two of the better CNT dispersants, NMP (N-methyl-pyrrolidone) and DMF (dimethylformamide) are ineffective graphene dispersants [22]. Chemically, the two materials are very similar, which suggests that it is the material geometry that is selecting for these solvents.

2.4 Systematic Searching

A trial-and-error approach has so far failed to yield good CNT or graphene solvents. More useful would be a systematic approach that could make predictions about the solvent quality of candidate molecules. One such approach that has been attempted is use of the Hansen solubility parameters [23].

The Hansen parameters are split into three components: a dispersive term (δ_d), a polar term (δ_p) and a hydrogen bonding term (δ_h). Solubility theory dictates that like will dissolve like and so a solvent should dissolve a solute if they have similar Hansen parameters. Several studies on CNTs and graphene [5, 10, 19, 24, 25] broadly agree that the dispersive parameter is most significant and the molecules with best dispersive power have a common δ_d, with δ_p and δ_h showing a much larger variability, suggesting they are less important.

The Hansen parameters are effective at ruling out potential solvents that do not have properties close to known dispersants. However they are less predictive when considering molecules with matching parameters; there are many non-solvents in this list. Understanding why the Hansen parameters struggle to make these predictions would undoubtedly be a step towards solving the problem of CNT and graphene dispersion.

Flory's solubility theory for rod like particles [26] can be used to estimate the concentration limit for carbon nanotube in solution. Bergin *et al.* [5] calculated a limit of 15 mg mL^{-1}

for isotropic solutions of single-walled carbon nanotubes (SWCNTs). This is not however an absolute solubility limit, a nematic phase occurs above this threshold [27]. Even so, there are no solvents that currently approach this isotropic limit, suggesting that there are still large improvements possible.

Torrens *et al.* [28, 29] conducted a study based on partition coefficients, and found that the CNTs preferred organic solvents over water, though absolute solubilities were still very small.

Pure water has been the subject of several MD simulation studies [30–32]. The results are conflicting, variously predicting solvent and non-solvent behaviour depending on the combination of forcefield and water model, perhaps related to the difficulty in parameterising water models for this particular application [33].

There have been several studies on solvent structure around individual tubes [34, 35]. While understanding of such structural information is crucial for the solvation process, and a significant amount of time is spent considering such in this thesis, it is also crucial to have corresponding free energy information.

2.5 The Potential of Mean Force, PMF

The PMF, $w(d)$, gives the distance dependence of the free energy (less an additive constant) of two particles. It is obtained from the mean force on the nano-particles $F(d)$, via integration

$$w(d) = -\int_{d}^{\infty} F(d)\partial d \; . \tag{2.1}$$

We define d as the surface to surface distance between two nano-particles. $F(d)$ is taken as the average of the absolute mean force on each nano-particle, and the sign is chosen so that a positive $F(d)$ points in the direction of increasing d.

In practice, we integrate from a distance, d^*, that is sufficiently far away that $F(d) = 0$ beyond d^*.

$$w(d) = -\int_{d}^{d^*} F(d)\partial d \tag{2.2}$$

The PMF gives us a free energy profile along increasing tube-tube distance, and is used to assess the quality of a solvent or dispersant from a simulation.

One of the difficulties in a wide ranging, systematic simulation study is the large computational load required for PMF calculations. The CDM technique presented here significantly reduces the resources required.

2.6 Solvents and Dispersants

There are two fundamental ways to keep an exfoliated CNT or graphene sheet stable in a solution: dispersion and dissolution. In a dispersion, a metastable dispersed state is created by the formation of an energy barrier between the individualised and the aggregated states (w_{reagg}, Figure 2.2). This *reaggregation barrier* slows the rate of reaggregation of the dispersed particles: thermal fluctuations in the system can provide energy for the system to climb the barrier and re-aggregate, but a sufficiently high barrier can stabilise a dispersion essentially indefinitely.

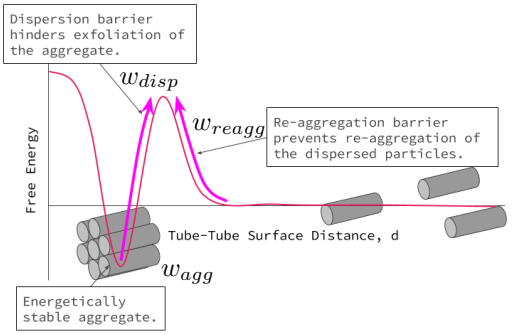

FIGURE 2.2: Typical free energy profile of a dispersant showing the dispersion (w_{disp}) and reaggregation (w_{agg}) barriers, and the aggregate energy (w_{agg}). The barriers in the system hinder the particles moving in in either direction.

The problem with a dispersant is that this re-aggregation barrier also acts in the opposing direction, and also creates an energy barrier to dispersing the material, and it is often larger than the re-aggregation barrier (w_{disp}, Figure 2.2). This *dispersion barrier* requires energy input to overcome.

Dissolution is characterised by the formation of a thermodynamically stable dispersed state, i.e. the dispersed state has a lower energy than the aggregate (Figure 2.3). This occurs if the solvent can more effectively replace the interactions between the target solute particles. In the absence of any energy barriers in the system, the solutes will spontaneously disperse in a thermodynamic solvent. A thermodynamic solvent would be the Holy Grail of CNT or graphene dispersion.

To avoid confusion going forward we will refer to *solvents*, the general class of chemical compounds, and *thermodynamic solvents*, compounds which produce a thermodynamically stable individualised solute.

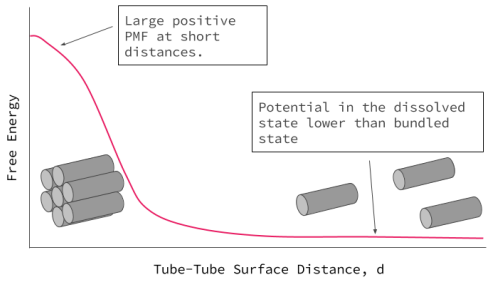

FIGURE 2.3: Typical free energy profile of a thermodynamic solvent. The particles in such a system will spontaneously separate.

2.7 The Un-Zippering Mechanism

The proposed un-zippering mechanism [36] provides a route from the aggregated to the individualised state that avoids an energy barrier. The mechanism was proposed for a carbon nanotube system but is equally applicable to similar materials.

If one end of a tube has managed to overcome the energy barrier to dispersion and has been separated from its bundle far enough, this end is in the individualised state. The contact region can now slide along the bundle without the need to overcome a barrier. However, this costs the (free) energy difference between the individualised and the aggregated state. For dispersants (that are not thermodynamic solvents) the aggregated state has a lower free energy compared to the individualised state. This means that energy has to be provided continuously during the entire exfoliation process. If this energy is not provided the reverse of the zippering mechanism does not only lead back to the bundled state but does so spontaneously and without a barrier, i.e. incompletely separated tubes snap back into contact with their bundles. The same applies to lateral sliding of the tubes. This means that dispersants are effective to stabilise dispersions of completely separated tubes, but they are detrimental to the separation process.

2.8 Summary

The problems of low yields, poor individualisation and ultra-sonication are common amongst all classes of current CNT and graphene solvents. These factors preclude any of these processes being used at an industrial scale, requiring thousands of litres of solvent for a few

kilograms of dispersed nanotubes with a huge amount of waste starting material, and requiring a sonication process which is difficult to scale up. The sonication process required by all current solvents is known to damage and shorten nanotubes [37, 38]. The electronic properties of the CNTs are then compromised by the introduction of defects to the surface, effectively doping the tubes. These same defects, combined with an overall reduction in length, also weaken their physical properties. It's reasonable to conclude similar problems will occur in graphene sheets under the effect of sonication.

It is these factors that motivate our search for solvents.

Bibliography

[1] Yu, M.-F., Lourie, O., Dyer, M. J., Moloni, K., Kelly, T. F., and Ruoff, R. S. (2000) Strength and Breaking Mechanism of Multiwalled Carbon Nanotubes Under Tensile Load. *Science 287*, 637–640.

[2] Tans, S. J., Verschueren, A. R. M., and Dekker, C. (1998) Room-temperature transistor based on a single carbon nanotube. *Nature 393*, 49–52.

[3] Jo, G., Choe, M., Lee, S., Park, W., Kahng, Y. H., and Lee, T. (2012) The application of graphene as electrodes in electrical and optical devices. *Nanotechnology 23*, 112001.

[4] Homaeigohar, S., and Elbahri, M. (2017) Graphene membranes for water desalination. *NPG Asia Materials 9*, e427.

[5] Bergin, S. D., Sun, Z., Rickard, D., Streich, P. V., Hamilton, J. P., and Coleman, J. N. (2009) Multicomponent Solubility Parameters for Single-Walled Carbon Nanotube-Solvent Mixtures. *ACS Nano 3*, 2340–2350.

[6] Zheng, L. X., O'Connell, M. J., Doorn, S. K., Liao, X. Z., Zhao, Y. H., Akhadov, E. A., Hoffbauer, M. A., Roop, B. J., Jia, Q. X., Dye, R. C., Peterson, D. E., Huang, S. M., Liu, J., and Zhu, Y. T. (2004) Ultralong single-wall carbon nanotubes. *Nature Materials 3*, 673–676.

[7] Clark, M. D., Subramanian, S., and Krishnamoorti, R. (2011) Understanding surfactant aided aqueous dispersion of multi-walled carbon nanotubes. *Journal of Colloid and Interface Science 354*, 144–151.

[8] Moore, V. C., Strano, M. S., Haroz, E. H., Hauge, R. H., Smalley, R. E., Schmidt, J., and Talmon, Y. (2003) Individually Suspended Single-Walled Carbon Nanotubes in Various Surfactants. *Nano Letters 3*, 1379–1382.

[9] Islam, M. F., Rojas, E., Bergey, D. M., Johnson, A. T., and Yodh, A. G. (2003) High Weight Fraction Surfactant Solubilization of Single-Wall Carbon Nanotubes in Water. *Nano Letters 3*, 269–273.

[10] Detriche, S., Zorzini, G., Colomer, J. F., Fonseca, A., and Nagy, J. B. (2008) Application of the Hansen solubility Parameters theory to carbon nanotubes. *Journal of Nanoscience and Nanotechnology 8*, 6082–6092.

[11] Bergin, S. D., Nicolosi, V., Streich, P. V., Giordani, S., Sun, Z., Windle, A. H., Ryan, P., Niraj, N. P. P., Wang, Z.-T. T., Carpenter, L., Blau, W. J., Boland, J. J., Hamilton, J. P., and Coleman, J. N. (2008) Towards Solutions of Single-Walled Carbon Nanotubes in Common Solvents. *Advanced Materials 20*, 1876–1881.

[12] Bergin, S. D., Sun, Z., Streich, P., Hamilton, J., and Coleman, J. N. (2010) New Solvents for Nanotubes: Approaching the Dispersibility of Surfactants. *The Journal of Physical Chemistry C 114*, 231–237.

[13] Chen, Q., Saltiel, C., Manickavasagam, S., Schadler, L. S., Siegel, R. W., and Yang, H. (2004) Aggregation behavior of single-walled carbon nanotubes in dilute aqueous suspension. *Journal of Colloid and Interface Science 280*, 91–97.

[14] Angelikopoulos, P., and Bock, H. (2012) The science of dispersing carbon nanotubes with surfactants. *Physical Chemistry Chemical Physics 14*, 9546–9557.

[15] Xu, Z., Yang, X., and Yang, Z. (2010) A Molecular Simulation Probing of Structure and Interaction for Supramolecular Sodium Dodecyl Sulfate/Single-Wall Carbon Nanotube Assemblies. *Nano Letters 10*, 985–991.

[16] Geng, H.-Z., Kim, K. K., So, K. P., Lee, Y. S., Chang, Y., and Lee, Y. H. (2007) Effect of Acid Treatment on Carbon Nanotube-Based Flexible Transparent Conducting Films. *Journal of the American Chemical Society 129*, 7758–7759.

[17] Paton, K. R. et al. (2014) Scalable Production of Large Quantities of Defect-Free Few-Layer Graphene by Shear Exfoliation in Liquids. *Nature Materials 13*, 624–630.

[18] Nicolosi, V., Chhowalla, M., Kanatzidis, M. G., Strano, M. S., and Coleman, J. N. (2013) Liquid Exfoliation of Layered Materials. *Science 340*, 1226419.

[19] Hernandez, Y. et al. (2008) High-yield production of graphene by liquid-phase exfoliation of graphite. *Nature Nanotechnology 3*, 563–568.

[20] Seo, J.-W. T., Green, A. A., Antaris, A. L., and Hersam, M. C. (2011) High-Concentration Aqueous Dispersions of Graphene Using Nonionic, Biocompatible Block Copolymers. *The Journal of Physical Chemistry Letters 2*, 1004–1008.

[21] Schlierf, A., Yang, H., Gebremedhn, E., Treossi, E., Ortolani, L., Chen, L., Minoia, A., Morandi, V., Samorì, P., Casiraghi, C., Beljonne, D., and Palermo, V. (2013) Nanoscale Insight into the Exfoliation Mechanism of Graphene with Organic Dyes: Effect of Charge, Dipole and Molecular Structure. *Nanoscale 5*, 4205–4216.

[22] Coleman, J. N. (2013) Liquid Exfoliation of Defect-Free Graphene. *Accounts of Chemical Research 46*, 14–22.

[23] Hansen, C. M. *The Three Dimensional Solubility Parameter And Solvent Diffusion Coefficient*; Danish Technical Press, 1967.

[24] Ham, H. T., Choi, Y. S., and Chung, I. J. (2005) An explanation of dispersion states of single-walled carbon nanotubes in solvents and aqueous surfactant solutions using solubility parameters. *Journal of Colloid and Interface Science 286*, 216–223.

[25] Cheng, Q., Debnath, S., O'Neill, L., Hedderman, T. G., Gregan, E., and Byrne, H. J. (2010) Systematic Study of the Dispersion of SWNTs in Organic Solvents. *The Journal of Physical Chemistry C 114*, 4857–4863.

[26] Flory, P. J. *Principles of Polymer Chemistry*; Cornell University Press: Ithaca, NY, 1953.

[27] Donald, A. M., Windle, A. H., and Hanna, S. *Liquid crystalline polymers*, 2nd ed.; Cambridge Univ. Press: Cambridge, 2006.

[28] Torrens, F. (2005) Calculations on solvents and co-solvents of single-wall carbon nanotubes: Cyclopyranoses. *Journal of Molecular Structure: THEOCHEM 757*, 183–191.

[29] Torrens, F. (2006) Calculations of organic-solvent dispersions of single-wall carbon nanotubes. *International Journal of Quantum Chemistry 106*, 712–718.

[30] Ou, S., Patel, S., and Bauer, B. A. (2012) Free Energetics of Carbon Nanotube Association in Pure and Aqueous Ionic Solutions. *The Journal of Physical Chemistry B 116*, 8154–8168.

[31] Zhang, Z., and Turner, C. H. (2014) Water-Induced Interactions between Boron-Doped Carbon Nanotubes. *The Journal of Physical Chemistry C 118*, 17838–17846.

[32] Ou, S.-C., and Patel, S. (2014) Electrostatic contribution from solvent in modulating single-walled carbon nanotube association. *The Journal of Chemical Physics 141*, 114906.

[33] Werder, T., Walther, J. H., Jaffe, R. L., Halicioglu, T., and Koumoutsakos, P. (2003) On the Water-Carbon Interaction for Use in Molecular Dynamics Simulations of Graphite and Carbon Nanotubes. *The Journal of Physical Chemistry B 107*, 1345–1352.

[34] Shim, Y., Jung, Y., and Kim, H. J. (2011) Carbon nanotubes in benzene: internal and external solvation. *Physical Chemistry Chemical Physics 13*, 3969–3978.

[35] Rana, M. K., and Chandra, A. (2015) Wetting behavior of nonpolar nanotubes in simple dipolar liquids for varying nanotube diameter and solute-solvent interactions. *The Journal of Chemical Physics 142*, 034704.

[36] Strano, M. S., Moore, V. C., Miller, M. K., Allen, M. J., Haroz, E. H., Kittrell, C., Hauge, R. H., and Smalley, R. E. (2003) The role of surfactant adsorption during ultrasonication in the dispersion of single-walled carbon nanotubes. *Journal of Nanoscience and Nanotechnology 3*, 81–86.

[37] Furtado, C. A., Kim, U. J., Gutierrez, H. R., Pan, L., Dickey, E. C., and Eklund, P. C. (2004) Debundling and Dissolution of Single-Walled Carbon Nanotubes in Amide Solvents. *Journal of the American Chemical Society 126*, 6095–6105.

[38] Rossell, M. D., Kuebel, C., Ilari, G., Rechberger, F., Heiligtag, F. J., Niederberger, M., Koziej, D., and Erni, R. (2013) Impact of sonication pretreatment on carbon nanotubes: A transmission electron microscopy study. *Carbon 61*, 404–411.

Chapter 3

Assessing the Quality of Solvents and Dispersants for Low-Dimensional Materials Using the Corresponding Distances Method

3.1 Copyright Statement

3.2 Introduction

The primary objective of this chapter is to demonstrate the corresponding distances method (CDM) for atomistic simulation; the technique having already been demonstrated for coarse grained simulation [1]. This was done by running a matching set of simulations using parallel tubes as a comparison. We demonstrate that the CDM can obtain very high resolution PMF curves at low computational cost in a single simulation. We also show that it provides all necessary structural information to interpret the structure/function relationship for the solvent.

As a secondary aim, it was also possible to explore, in detail, the behaviour of $CBrCl_3$ as a solvent of carbon nanotubes through analysis of the potential of mean force (PMF) and its origins in the structure and orientational configuration of $CBrCl_3$ around CNTs.

$CBrCl_3$ was chosen as a test case out of a set of several dozen solvents studied by Bergin *et al.* [2]. It is interesting for two reasons: $CBrCl_3$ has a simple structure which makes subsequent analysis of any structural details in simulation much easier; and it was predicted as a solvent by the Hansen solubility parameters, despite dispersing no tubes in experiment.

In this chapter we will demonstrate that the corresponding distances method, previously shown to be effective in course grained simulation [1], in atomistic molecular dynamics can be used in conjunction with atomistic models to

3.3 Theoretical Methods

Ad discussed in Section 2.5, we will use the potential of mean force (PMF, $w(d)$) to assess the quality of solvents and dispersants from our simulations. The forces $F(d)$ needed to calculate the PMF can be obtained from a series of simulations with two parallel tubes at varying distance d, where $F(d)$ is the ensemble average of the sum of the forces (parallel to d) acting on all the carbon atoms on one of the tubes.

Due to the high symmetry of the nanotubes one would obtain the same force *per tube length* for each of the periodic rings of carbon atoms (Figure 3.1) as for the entire tube, although sampling would have to be increased proportional to the reduction in tube length considered.

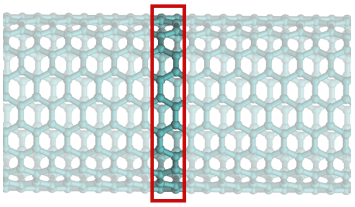

FIGURE 3.1: Schematic of a (10,10) armchair carbon nanotube. Highlighted is the double ring of carbon atoms that represents the smallest repeat unit along the tube axis.

The general idea of the corresponding distances method is to create a system where all tube/tube distances are present at the same time. [1] The simplest way to achieve this is to use two tubes that cross at a small angle (bottom panel of Figure 3.2). The forces on the horizontal tube are calculated in the same way as for the parallel tubes but for each ring of carbon atoms separately. The distance to the other tube that is associated with each of the rings is determined as shown in Figure 3.2, i.e. it is given by the distance to the first solvent layer added to the (shortest) distance from the first solvent layer to the other tube.

The CDM is clearly an approximation, however, it performs very well for coarse-grain models [1] and below we demonstrate its excellent performance for an atomistic model.

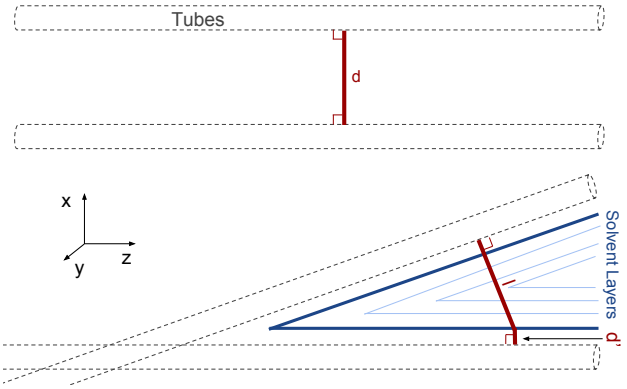

FIGURE 3.2: Schematic of the two system setups used (top: parallel, bottom: CDM). The link between the two systems is established by the corresponding distance, $d = l + d'$

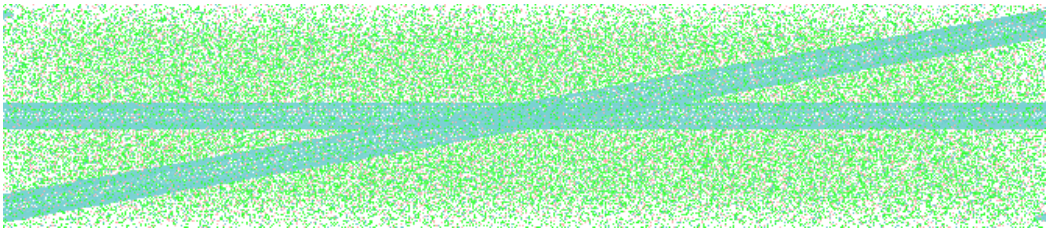

FIGURE 3.3: Top-down snapshot of the $CBrCl_3$/ CNT system used for the CDM.

3.4 Simulation

Molecular dynamics simulations were run using the GROMACS 5.1 simulation package [3–9].

Initial box dimensions for each of the simulations with parallel tubes were: $x = 12.00$nm, $y = 12.00$nm, $z = 24.59512$nm, with the two parallel tubes placed in the $x, y = 0, z$ plane and the tube axes oriented along the z-axis (Figure 3.2, top). Each of the tubes had $4,000$ atoms. The number of solvent molecules varied between simulations (due to the increasing excluded volume of the tubes as they move apart) but was approximately $18,500$, giving a total system size of circa $101,000$ atoms.

In the corresponding distances method the two tubes are angled to one another (bottom panel of Figure 3.2). Here the axis of one of the tubes coincides with the z-axis while the other one is rotated from this position around the y-axis by $10°$. Thus, the two tubes are still in the $x, y = 0, z$ plane but cross in the centre of the box.

Complete periodicity is maintained for the horizontal tube, while the rotated tube has defects at the edges of the system, which are irrelevant for the force calculation. The initial box dimensions for the CDM simulation were: $x = 10.8480$nm, $y = 61.4716$nm, $z = 6.0000$nm. The horizontal tube of the CDM simulation had $10,000$ atoms, the rotated tube had $10,160$ atoms and there were $20,612$ solvent molecules, giving $123,220$ atoms in total.

Very similar simulation procedures were followed for both systems. Once the tubes have been placed in the box, the space is filled by overlaying repeat units of a pre-equilibrated solvent box. All solvent molecules that overlap with or are located inside the tubes are removed. After an initial energy minimisation step (EM), a short temperature equilibration step was performed (NVT), followed by a pressure coupled equilibration phase (NPT). During (NPT) equilibration the box dimensions were only allowed to deform in the dimensions that were not coupled to the tube lengths, i.e. x and y for the parallel simulations and only y for the CDM simulation (Figure 3.2). The last step is the (NVT) production run to collect data for analysis.

All simulations were conducted at atmospheric pressure (1 bar) and a temperature of 300 K. The remaining simulation parameters are collated in Table A.1.

3.4.1 Model and Force Field

The forcefield used was GROMOS 53a6 [10]. Parameterisation of the solvent was done with the aid of the Automated Topology Builder [11–13] and manually verified.

The tubes used in this study are (10,10) armchair CNTs with a diameter of 1.36nm. The nanotubes were built with the aid of the Buildcstruct script [14] and were given the same non-bonded characteristics of a standard carbon atom in the GROMOS 53a6 force field. The parameters for the solvent and nanotubes can be found in the Supporting Information.

The CNTs are approximated as rigid rods, i.e. the CNT atoms are “frozen" in place. In the simulations the tube atoms are treated normally, but their positions are never updated.

In the solvent simulations no inter- or intra-tube C/C interactions are considered. Thus the direct tube/tube interaction contribution to the PMF is calculated separately using the same techniques with a single step MD simulation in a vacuum using the forcefield’s base C-C potential for the inter-tube interactions.

Like many other force fields, GROMOS 53a6 is a biomolecular forcefield in origin. It was parameterised to match free energies of solvation of amino acids (in water and cyclohexane) and to reproduce the properties (density and heat of vaporisation) of a range of small solvent molecules. These two criteria are in line with the goals of the work in this thesis. The force field was also shown to reproduce the tube-tube potential for (10,10) carbon nanotubes [15]. Thus we believe that the force field is applicable for our purposes.

3.5 Results and Discussion

3.5.1 Corresponding Distances Method

The PMF, $w(d)$, was computed from a tube-tube distance of $d = 4$ nm. We refer to this as the *dispersed* or *individualised* state. The *bundled* or *aggregated* state occurs around the minimum in the direct tube/tube interaction of $d \approx 0.33$nm.

The solvent mediated PMF (smPMF) of a pair of (10,10) swCNTs is presented in Figure 3.4. To obtain Figure 3.4 we performed 40 individual simulations of two parallel nanotubes at varying d. Maintaining thermodynamic consistency across these 40 simulations is challenging, the computational resources required are large, and it is also not possible to know *a priori* where data points are needed in order to produce an accurate PMF.

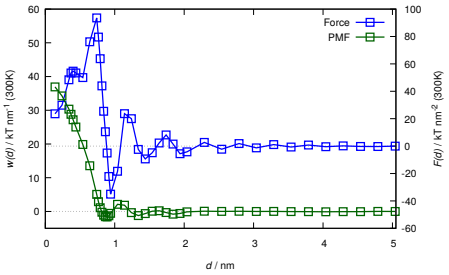

FIGURE 3.4: The solvent-mediated part of the potential of mean force $w(d)$ (green) and the associated mean force $F(d)$ (blue) as a function of the surface-to-surface distance d between a pair of parallel (10,10) tubes obtained from individual simulations at various distances d.

Figure 3.5 shows the effects of missing data points on the integration of the force data to obtain the smPMF. In the initial dataset (turquoise crosses), the smPMF is negative across a large range between $d = 1$ nm and $d = 2$ nm. Adding just 6 data-points and recalculating the smPMF yields the final, correct, dataset (green squares). These 6 added data-points corresponded with very small oscillations in the force, but because they are integrated across a large d interval they make a large contribution to the smPMF. Without another source to verify the smPMF, it would have been difficult to tell that the initial result was incorrect.

We have developed the corresponding distance method (CDM) [1] to solve the above problems. The CDM calculates the entire smPMF in one simulation, guaranteeing thermodynamic consistency across all d as they are connected to the same bulk. The smPMF is calculated at high resolution, eliminating integration problems, and because we have reduced the amount of bulk solvent, computational efficiency is greatly improved.

The CDM is an approximation, though the comparisons in Figure 3.6 demonstrates its excellent performance. The smPMF from the CDM (Figure 3.6b, magenta line) is calculated from 400 individual data points compared to the 40 from the parallel simulations. With so

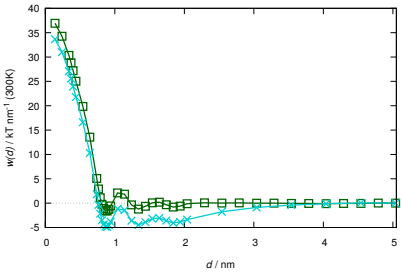

FIGURE 3.5: The smPMF for $CBrCl_3$ as calculated from an initial dataset (turquoise crosses), compared to the final smPMF calculated using 6 additional data points (green squares).

many data points we do not have to worry about integration errors when calculating the smPMF from the CDM.

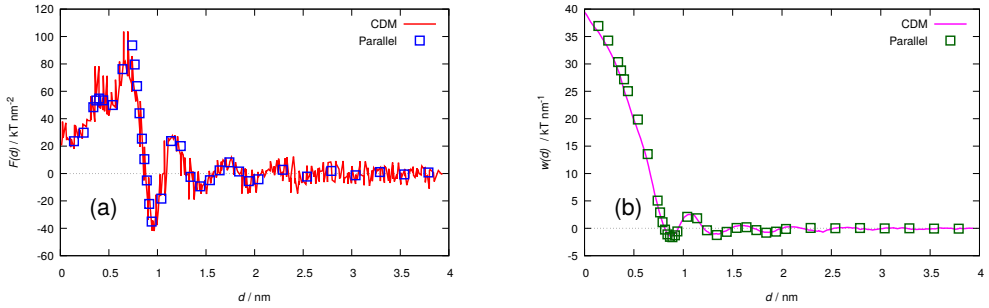

FIGURE 3.6: The solvent-mediated force $F(d)$, (a), and the solvent-mediated part of the potential of mean force $w(d)$, (b), as a function of tube/tube distance, demonstrating the excellent performance of the corresponding distance method. Solid lines represent results from the corresponding distance method, while the data indicated by open symbols has been obtained from individual simulations of systems comprising pairs of parallel carbon nanotubes.

The CDM requires less than a tenth of the computational resources needed to achieve the same by simulating individual systems of parallel tubes. The savings originate primarily from eliminating the need to equilibrate a large number of small systems, from reduction of the total bulk liquid that needs to be simulated and from reducing the total size of the "systems" at each distance because periodic boundary conditions don't apply.

The corresponding distance method makes the calculation of high resolution PMF curves routine.

3.5.2 Bromotrichloromethane, $CBrCl_3$

Using Hansen's solubility parameters, solutes with dispersive (δ_D), polar (δ_P) and hydrogen bonding (δ_H) parameters similar to a solvent, will dissolve in that solvent. CNTs have shown not to follow this behaviour, having been determined by Bergin *et al.* [2] to have

similar parameters (Table 3.1) to $CBrCl_3$ despite being completely insoluble. We will use the CDM to determine the origin of the poor performance of $CBrCl_3$.

Molecule	$C_{\max}$ mg/mL	δ_D MPa$^{-\frac{1}{2}}$	δ_P MPa$^{-\frac{1}{2}}$	δ_H MPa$^{-\frac{1}{2}}$
$CBrCl_3$	0	18.3	8.1	6
dibenzyl ether	0	19.6	3.4	5.2
acetone	0.011	15.5	10.4	7.0
DMPU	0.65	17.8	9.5	9.3
CHP	3.5	18.2	6.8	6.5
weighted average best 14 molecules		18.0	7.8	6.9

TABLE 3.1: Hansen parameters and CNT dispersibility for $CBrCl_3$ and a selection of other molecules taken from Data taken from Ref. [2], as well as the weighted average of the top 14 solvents. The additional solvents are shown to demonstrate the range of Hansen parameters and similarity of $CBrCl_3$ to good CNT solvents (CHP and DMPU) and difference to other poor solvents (acetone and dibenzyl ether).

Figure 3.6a (red line) shows the $CBrCl_3$ mediated forces between two nanotubes as measured from the CDM simulation. The force curve can be split into three regions: a large repulsive region at small d, followed by some oscillations, with the force going to zero at large d.

The noise observed in the force curve is a result of averaging over only a few carbon atoms at each tube-tube distance. However, because of the high resolution of the force curve, this noise is not inherited by the smPMF (Figure 3.6b, magenta curve).

The oscillations between around $d = 0.8$ nm and $d = 2.5$ nm are caused by the ordering of solvent molecules around the nanotubes. This ordering is clearly visible in density maps of carbon atoms in the system as shown in Figure 3.7. This figure also demonstrates that the structural information from the CDM is the same as that calculated using a pair of parallel tubes.

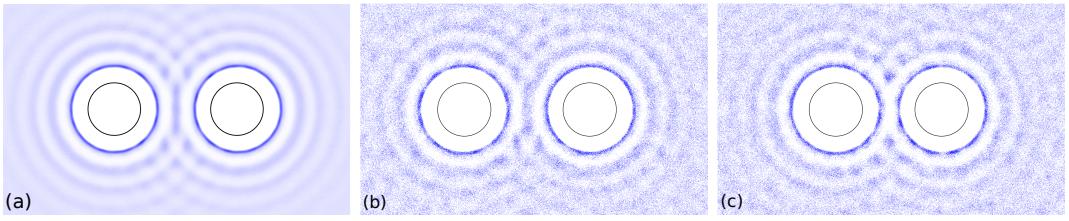

FIGURE 3.7: Local densities of carbon atoms at $d = 1.84$nm, (a, b) and $d = 1.34$nm highlighting solvent layering and the squeeze-out of a solvent layer from (b) to (c). Results form the CDM (b, c) and the simulation of parallel tubes are identical apart from better averaging for the latter. Scale bars are provided in Appendix B.

The solvent molecules between the tubes are confined. At zero force, a given number of layers between the tubes are in a stable configuration: if the tubes were not already held in place by the simulation, they would not be moved by the solvent-mediated forces. As the tube/tube distance, d, is reduced from this point, the confined solvent is compressed and exerts a

repulsive force on the tubes, pushing them apart. If we decrease d too much, the current layering configuration becomes unstable and one layer is squeezed out (*c.f.* Figure 3.7b and Figure 3.7c). $CBrCl_3$ does not experience strong layering beyond the first layer, resulting in only small oscillations beyond $d \approx 1$ nm of a few kT nm^{-1} in the smPMF.

The first solvent layer (closest to the tubes) has a high density, suggesting strong adherence to the tube surface. This layer strongly resists being squeezed out by the other approaching nanotube with a much greater force than any of the other layers and over a longer distance. This gives an extended region where the smPMF is positive at $d < 0.88$ nm, where the solvent acts to push the tubes apart.

This repulsive region is key to determining the solvent and dispersant quality of a molecule as it is here the smPMF overlaps with the strongly attractive region of the tube-tube PMF (ttPMF). The two contributions (smPMF and ttPMF) and the combined PMF are shown in Figure 3.8.

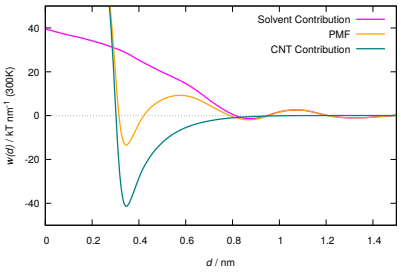

FIGURE 3.8: The full potential of mean force (yellow) and its two additive contributions, the direct tube/tube interaction (green) and the smPMF (magenta), showing that, while the aggregated state has been weakened, it remains stable and that a barrier is formed between the aggregated and the dispersed states.

It can be clearly seen that $CBrCl_3$ has a significant destabilising effect on the aggregated state, reducing the aggregate energy from around -40 kT nm^{-1} at $d \approx 0.33$ nm in a vacuum to -12 kT nm^{-1} immersed in the solvent. However, it does not destabilise the aggregate completely and the aggregate energy remains below that of the dispersed state, the tubes will not spontaneously separate and $CBrCl_3$ is not a thermodynamic CNT solvent.

Further out at $d = 0.58$ nm, an energy barrier appears, with a maximum of 11 kT nm^{-1}. This kind of barrier is characteristic of a dispersant, separating the dispersed and aggregated states. It must be overcome for separated tubes to create a bundle. However, the barrier operates in both directions and is twice as large (23 kT nm^{-1}) when considering separating an already aggregated pair of tubes. How significant this barrier is depends on the exact de-bundling process.

In the proposed un-zippering mechanism [16] (Section 2.7), the energy barrier need only be overcome during the activation process. Because the aggregated state of the CNTs in $CBrCl_3$

is energetically favoured, we would then require a constant application of energy (equal to the difference between the dispersed and aggregated states) until the tubes are fully separated, or they will snap back to the aggregated state. Once the tubes are separated, we require a sufficiently large barrier to prevent thermal fluctuations in the system providing the tubes with the energy necessary to cross it and re-aggregating spontaneously.

If the initial barrier is too large, if we can't continuously apply energy to the dispersing region, or if the re-aggregation barrier is too small, then the dispersant will not be effective.

In the dispersed state the tubes are (more or less) randomly orientated. In general, we would expect the re-aggregation barrier to decrease with decreasing contact area, making the case where two tubes approach at 90° the most vulnerable to re-aggregation. With a 1.36 nm diameter, we estimate our tubes to have a re-bundling barrier of about 15 kT nm^{-1}at 90°. This is probably too low to stabilise a dispersion considering that this is only the *average* barrier height and fluctuations in the system will mean it is lower in places: once one section of tube has re-aggregated, the rest can proceed barrier-less.

3.5.3 Structure-Function Relationship

We start with analysis of the structure-function relationship of $CBrCl_3$ around a single, isolated carbon nanotube. The number of solvent atoms versus distance to the tube surface curves, N(r), as presented in Figure 3.9b, clearly shows the layered structured of the solvent. The first layer shows specific, intense structuring of individual solvent atoms indicating a preferential orientation of the solvent molecules at the tube surface. From the second layer onwards, beyond $d \approx 0.7$ nm, the molecules appear to be randomly orientated: all three N(r) peaks are broad and located at the same position.

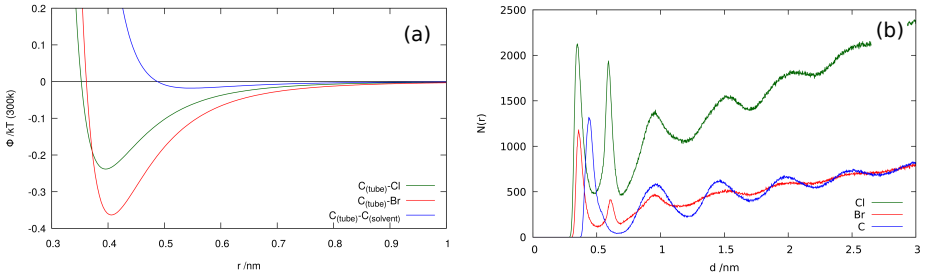

FIGURE 3.9: Tube carbon to solvent atom van der Waals interactions (a) and N(r), the number of solvent atoms as a function of distance from the surface of an individual nanotube (b). Part (b) indicates layering and intense orientational order of the solvent molecules in the first layer.

In the first layer, within $d \approx 0.7$ nm, for each carbon atom there is approximately one bromine and two chlorine atoms located slightly close to the tube. The fourth halogen atom

points away from the tube, indicated by a second large chlorine peak beyond the carbon peak. This is usually a chlorine atom: the C-Br Lennard Jones strength parameter is large than that of C-Cl (Figure 3.9), and so the bromine atom is preferentially adsorbed to the tube surface. The distance between the first carbon peak and this second chlorine peak is 0.156 nm which is consistent with the C-Cl equilibrium bond length of 0.176 nm in $CBrCl_3$.

We can determine that the $CBrCl_3$ molecules adsorb with their triangular base on the tube surface, consistent with the expectation that the molecules tend to maximise their adsorption energy. We can also see the exact opposite configuration occasionally occurs, but at a much lower incidence. Both of these orientations (as well as a handful of much less prevalent ones) can be seen with careful inspection of the simulation snapshot in Figure 3.10. Note that the Cl atoms are located slightly closer to the tubes compared to the Br atoms because the Cl/C van der Waals interaction is slightly shorter ranged (Figure 3.9a).

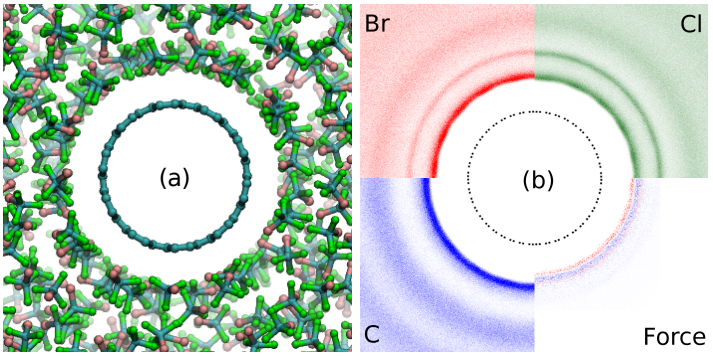

FIGURE 3.10: Snapshot (a) and local densities for all solvent atom types (b) visualising the solvent structure around an individual carbon nanotube. Shown is also a force map (b, bottom right quadrant) highlighting that most of the force between the tube and the solvent originates from the atoms closest to the tube. Stronger colours indicate higher density and force. In the force map repulsive forces are shown in red and attractive forces in blue. Scale bars are provided in Appendix B.

It is instructive to briefly consider the interactions between the solvent and the nanotube. In Figure 3.10b the local solvent/nanotube force at the location of the solvent atoms is shown. A significant part of the total force is repulsive, which is expected as the tube/solvent interface must sustain the external pressure. These repulsive interactions are shared between the Cl and Br atoms in the base of the adsorbed tetrahedron, while the atom pointing away from the tubes contributes only little. Note, that the interaction with the carbon atoms is relatively small, but contributes attractively and repulsively due to its relatively long range (Figure 3.9a).

The orientation of the adsorbed solvent molecules in the first layer determines the strength and range of the solvent mediated forces generated as two tubes approach. These forces result in the repulsive region in the smPMF, which in turn determines the solvent or dispersant

quality of the molecule. Understanding this structure-function relationship between the solvent and the smPMF is crucial to crucial for an informed solvent design process.

The repulsive region of the solvent-mediated (average) tube/tube force $F(d)$ begins at $d = 0.88$nm, where the force is zero and the smPMF has a minimum (Figures 3.6 and 3.8). At this particular distance a single layer of solvent molecules is sandwiched between the tubes as can be observed by following the ring structure in the local density (top row in Figure 3.12) and by inspection of the snapshot shown in Figure 3.11. We expect this layer to be largely unstrained, which is consistent with the observation that the molecules in the confined region retain the orientation they assume in the unconfined part of the adsorbed layer (compare also to Figure 3.10a).

However, in this configuration the atom at the top of the adsorbed tetrahedron can now interact with the other tube. This is possible only at very specific positions, which causes lateral structuring of the confined layer. The formation of two distinct rows of solvent molecules either side of the centre of the gap between the tubes is particularly obvious in the local densities of the carbon atoms (middle of top row in Figure 3.12).

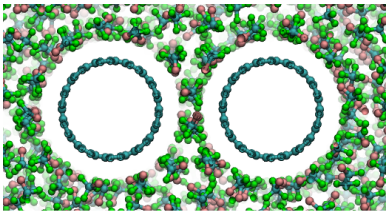

FIGURE 3.11: Snapshot of a thin slice of the CDM system at $d = 0.88$nm. Clearly visible is the structuring of the confined solvent layer into two rows of molecules running along the tubes.

When the distance between the tubes is reduced, the confined layer is compressed and the two rows of molecules are pushed out of the gap (second row of Figure 3.12) which results in a repulsive restoring force. Thus, the size of the repulsive region is determined by the geometry of the solvent molecules.

To analyse the specific behaviour of the nanotube/$CBrCl_3$ system in the repulsive region of $F(d)$ it is instructive to consider a simpler proxy (Figure 3.13). At the point where the adsorbed first layers of the two tubes overlap and terminate, they push the two rows of molecules between the tubes like a wedge (magenta). The responsible force (red arrows in Figure 3.13) originates from the "lateral adsorption pressure" in the adsorbed layers.

As the force contributions from the two layers are mirror symmetric with respect to the centre of the tube/tube contact, their x-components cancel, while their y-components add. Thus, the resulting force that pushes the wedge between the tubes only has a y-component.

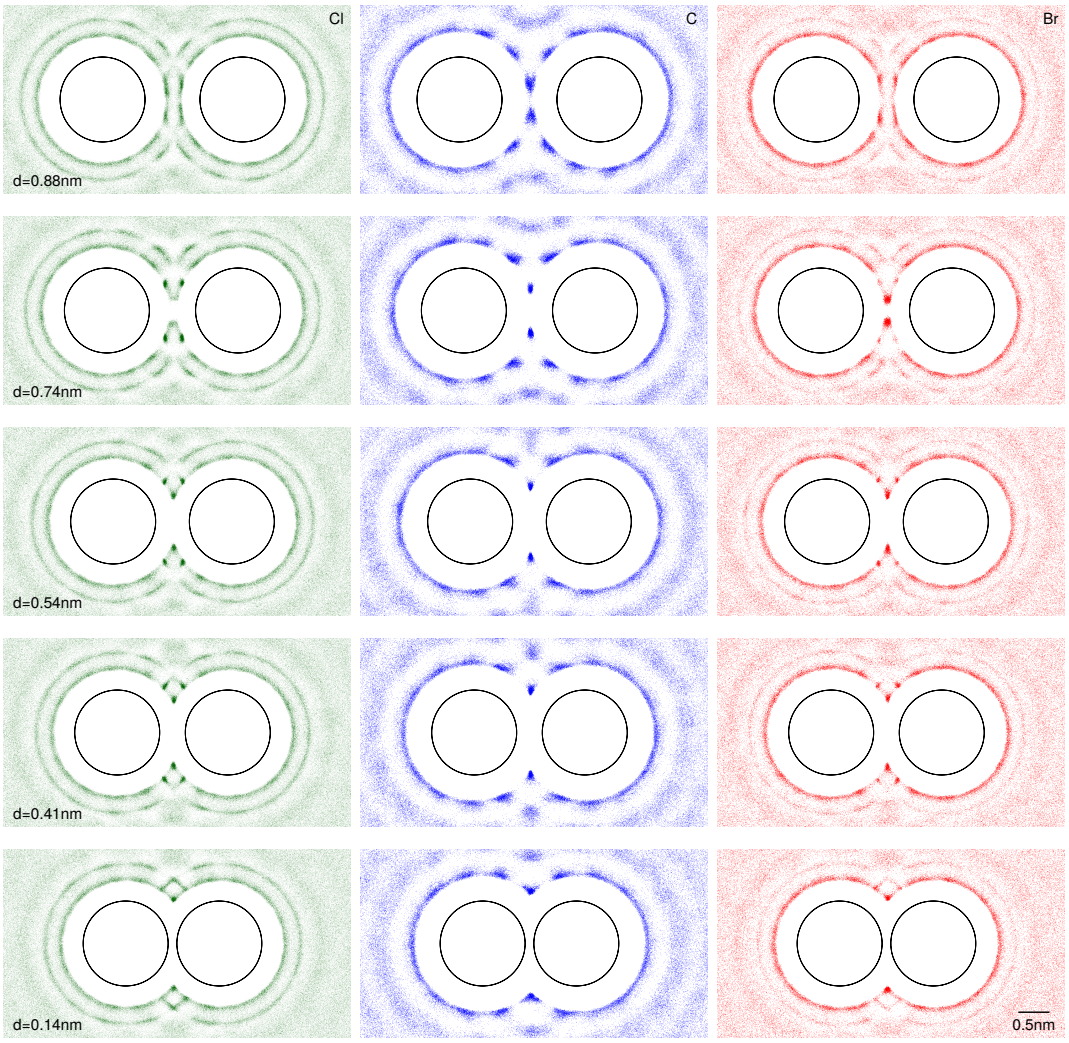

FIGURE 3.12: Local densities of the solvent atoms at various distances d as indicated in the figure. Note that the Cl density has been scaled down by a factor of 3. Scale bars are provided in Appendix B.

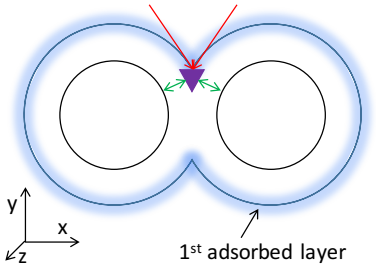

FIGURE 3.13: Schematic introducing the "wedge" model. The wedge is shown in purple. The arrows indicate the tube/wedge force (green) and the force with which the adsorbed layers push the wedge into the gap between the tubes (red). Only the top wedge is indicated.

At equilibrium this force must be balanced by the wedge/nanotube forces (green arrows in Figure 3.13). These forces also have x-components which cancel due to the same symmetry.

Vitally, although the x-components of the two wedge/nanotube forces cancel at the wedge, they are counterbalanced by different tubes and therefore push them apart. This is one contribution to $F(d)$.

In a very similar way the x-components of the forces pushing the wedge into the gap between the tubes (red arrows in Figure 3.13) must also be counterbalanced by the tubes. These x-components cause the two layers to deform and/or shift slightly in the $-x$ and $+x$ direction for the left and right tube, respectively, which creates the required counterbalancing forces. These forces are the second contribution to $F(d)$.

This means that much of the profile of the repulsive region of $F(d)$ is governed by the geometry of the tubes which determines the angle at which the adsorbed layers interact with the wedge (angle between red arrows in Figure 3.13). In addition to this, the geometry of the wedge, i.e. the exact geometry of the solvent molecules in the two adsorbed rows, makes a contribution via the orientation of the nanotube/wedge force (angle between green arrows in Figure 3.13). In general we expect that when the distance between the tubes is reduced the repulsive force decreases as the wedge moves out of the gap and the geometry becomes less favourable.

Using this model we find that at $d \approx 0.74$nm the solvent-mediated force $F(d)$ in Figure 3.6a is high because the two rows of molecules that from the “wedge" are located deep in the gap between the tubs resulting in a large y-component of the force from the adsorbed layers on the wedge and a large x-component of the wedge/nanotube force, which consequently leads to the large value of $F(d \approx 0.74\text{nm})$.

At $d \approx 0.74$nm the wedge molecules have increased their order slightly compared to $d \approx 0.88$nm and are now oriented in such a way that the bromine atom is located at the tip of the gap formed by the two tubes, while the three chlorine atoms face outward. Two of the Cl atoms are adsorbed on one tube with the third on the other tube (second row of Figure 3.12). In this conformation the wedge formed by the molecules is too blunt for the gap between the tubes. Consequently, the chlorine atoms sustain the repulsive force with the tubes (Figures 3.14 and 3.15), while the bromine atom “dangles” in the gap as can be seen by the rather broad Br spot in the local density in combination with quite sharp Cl and C spots (second row of Figure 3.12).[1]

[1] Although the C atom of $CBrCl_3$ is well shielded by the halogen atoms, the force-field assigns a repulsive interaction with the tubes (see Figure 3.9a) and Figure 3.14). This rather long range repulsion may be an artefact of the force-field caused by using an LJ(12,6) for van der Waals type interactions for all atoms. However, the contributions of the C atom of $CBrCl_3$ to the tube/tube force is consistent with that of the halogen atoms and does not affect the presented interpretation of the forces.

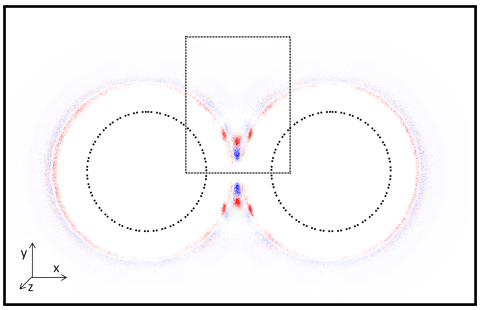

FIGURE 3.14: x-component of the local forces at $d = 0.74$nm showing the location of atoms that interact with the tubes repulsively (red) or attractively (blue). The tubes are shown as a solid black line. The area marked by the dashed rectangle is enlarged in Figure 3.15. Scale bars are provided in Appendix B.

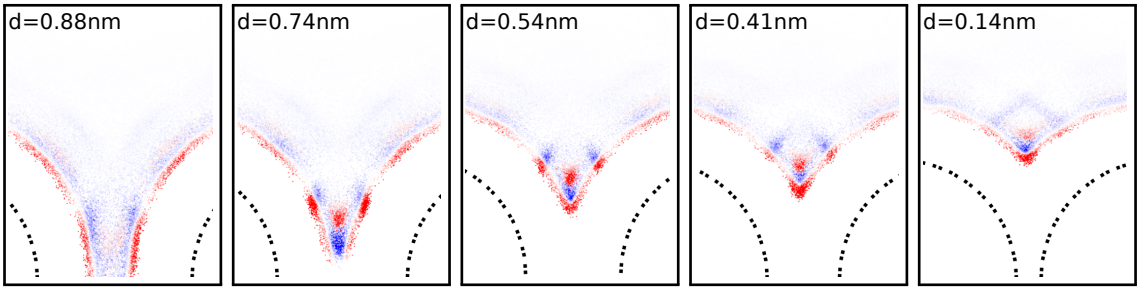

FIGURE 3.15: Same as Figure 3.14 but showing an enlarged area at various tube/tube distances corresponding to Figure 3.12. Scale bars are provided in Appendix B.

As d is reduced further, the gap between the tubes becomes shallower. This means that eventually the Br atom will interact with both tubes and sustain most of the repulsive tube/wedge force. This is a more favourable geometry for a large value of $F(d)$, as the Br atom lies deeper in the gap than the Cl atoms (Figures 3.12 and 3.16). However, simultaneously the wedge is being pushed out quickly with reducing d, which appears to overcompensate the previous effect.

Interestingly there is a second rather broad maximum around $d = 0.41$nm. This can only be caused by the wedge molecules as the tubes don't have any non-monotonous geometrical features.

At $d \approx 0.41$nm the wedge has moved still further out of the gap as is evident from the location of the carbon atoms (row 4 of Figure 3.12). However, the molecule has rotated such that two halogen atoms (including bromine) point into the gap and interact with both tubes simultaneously while the other two chlorine atoms point outward and each interact with a different tube. This amounts to 6 tube/halogen interactions as compared to 5 found in the configuration at $d \approx 0.74$nm. It is likely that this increase drives the reorientation of the molecules that form the "wedge". (Note that the tube/atom interaction energy can be negative although the associated force is repulsive).

In this orientation of the molecules the wedge is slightly more blunt than before, but also the gap between the tubes has become more blunt until at $d \approx 0.41$nm the wedge is sharper than the gap and therefore interacts repulsively with the tubes at is tip (Br, Cl) as opposed to the repulsive interactions at its heel at larger d (sequence in Figure 3.16). This moves the interaction centre slightly further into the gap and to a more favourable geometry, which appears to be responsible for the slight increase in the solvent-mediated tube/tube force at $d \approx 0.41$nm.

Decreasing the distance between the tubes pushes the wedge molecules further out of the gap between the tubes, which makes the geometry less favourable for strong solvent-mediated tube/tube repulsion. The atoms at the tip of the wedge continue to sustain the repulsive force while only one of the other two halogen atoms can continue to interact with a tube.

From the discussion above it is clear that strong adhesion between the solvent molecules and the nanotubes is essential for a strong repulsive region in $F(d)$. However this strong adsorption should not lead to a deep first minimum in the smPMF. Indeed, $CBrCl_3$ only has a very shallow first minimum (Figure 3.8). The reason for this is likely the strong asymmetry of its interaction with the tubes; when one layer is stable between the tubes four atoms interact with one tube while only one interacts with the other.

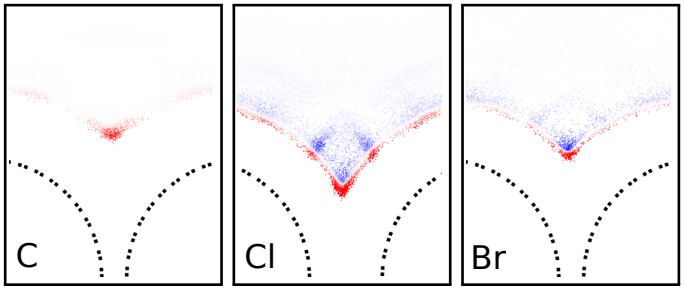

FIGURE 3.16: Same as figure 3.14 but showing an enlarged area for $d = 0.41$nm and split into contributions from the three solvent atom types as indicated in the figure, showing that the repulsive forces are sustained by Cl and Br, while C never comes close enough to the tubes to interact repulsively. Scale bars are provided in Appendix B.

3.6 Conclusion

3.6.1 The Corresponding Distances Method

We have demonstrated the corresponding distance method as a useful tool to investigate solvents and dispersant for low dimensional materials. It is able to produce higher resolution, accurate potential of mean force curves, with much greater computational efficiency than standard methods.

We applied the corresponding distance method to investigate the solvent and dispersant quality of $CBrCl_3$. Bergin *et al.* [2] used the predicted solubility parameters of swCNTs to wrongly predict $CBrCl_3$ as a solvent. Our results show that while $CBrCl_3$ reduces the stability of the bundled state from -40 kT nm^{-1} to -12 kT nm^{-1} it can not destabilise it completely. It is therefore not a solvent in the thermodynamic sense.

$CBrCl_3$ creates a barrier of 11 kT nm^{-1} between the individualised and the bundled states in the re-aggregation direction. This is for parallel tubes, the true barrier for the most vulnerable, i.e. the 90°, configuration is likely to lie below 15kT on average. This is unlikely to be sufficient to stabilise a CNT dispersion and might be reduced even further temporarily by thermal fluctuations of the adsorbed solvent layers.

Our finding that $CBrCl_3$ is neither a good solvent nor a good dispersant for swCNTs is consistent with experimental results [2].

It is worth nothing that our simulations only calculate the PMF between two particles. In principle, the PMF is additive, i.e. the energy to separate four tubes is twice that would be required to separate two. However, this does not account for many-body effects introduced by additional particles. We have seen how the solvent density layers interfere with each-other to produce the shape of the smPMF. A third density wave would change this density interference pattern and may change the smPMF in ways that cannot be wholly predicted just by consideration of the two-particle problem. These many-body interactions introduce a large number of additional dimensions, and while no doubt an interesting study, they remain beyond the scope of what we are able to investigate in this thesis.

3.6.2 Lessons for Solvent Design

From this chapter we can learn several lessons for solvent design. Firstly, the solvent-mediated PMF must be greater than 40 kT nm^{-1} at the tube/tube equilibrium distance in order to compensate the tube/tube potential. Ultimately this energy must be raised by solvent adsorption from the liquid. At the same time this required adsorption must not lead to a strong free energy minimum at one solvent layer sandwiched between the tubes. It is this dependence of the behaviour of the solvent molecules on the tube structure that the solubility parameters can not capture.

Secondly, the barrier between the bundled and the dispersed state should ideally be removed. In a thermodynamic solvent, any barrier here only serves to hinder the dispersion process. Removing this barrier requires one to shorten the range of the solvent-mediated repulsion to match the range of the direct tube/tube attraction. This in turn requires the molecule or fragment that is inserted between the tubes to be small and/or flat.

Bibliography

[1] Müter, D., and Bock, H. (2014) Interactions between Nanofibers in Fiber-Surfactant Suspensions: Theory of Corresponding Distances. *Physical Review Letters 112*, 128301.

[2] Bergin, S. D., Sun, Z., Rickard, D., Streich, P. V., Hamilton, J. P., and Coleman, J. N. (2009) Multicomponent Solubility Parameters for Single-Walled Carbon Nanotube-Solvent Mixtures. *ACS Nano 3*, 2340–2350.

[3] Van Der Spoel, D., Lindahl, E., Hess, B., Groenhof, G., Mark, A. E., and Berendsen, H. J. C. (2005) GROMACS: Fast, flexible, and free. *Journal of Computational Chemistry 26*, 1701–1718.

[4] Pronk, S., Páll, S., Schulz, R., Larsson, P., Bjelkmar, P., Apostolov, R., Shirts, M. R., Smith, J. C., Kasson, P. M., Spoel, D. v. d., Hess, B., and Lindahl, E. (2013) GROMACS 4.5: a high-throughput and highly parallel open source molecular simulation toolkit. *Bioinformatics 29*, 845–854.

[5] Abraham, M. J., Murtola, T., Schulz, R., Páll, S., Smith, J. C., Hess, B., and Lindahl, E. (2015) GROMACS: High performance molecular simulations through multi-level parallelism from laptops to supercomputers. *SoftwareX 1–2*, 19–25.

[6] Hess, B., Kutzner, C., van der Spoel, D., and Lindahl, E. (2008) GROMACS 4: Algorithms for Highly Efficient, Load-Balanced, and Scalable Molecular Simulation. *Journal of Chemical Theory and Computation 4*, 435–447.

[7] Páll, S., Abraham, M. J., Kutzner, C., Hess, B., and Lindahl, E. In *Solving Software Challenges for Exascale*; Markidis, S., and Laure, E., Eds.; Lecture Notes in Computer Science 8759; Springer International Publishing, 2014; pp 3–27.

[8] Erik Lindahl,, Berk Hess,, and Spoel, D. v. d. (2001) GROMACS 3.0: A package for molecular simulation and trajectory analysis. *J. Mol. Model* 306–317.

[9] Berendsen, H. J. C., van der Spoel, D., and van Drunen, R. (1995) GROMACS: A message-passing parallel molecular dynamics implementation. *Computer Physics Communications 91*, 43–56.

[10] Oostenbrink, C., Villa, A., Mark, A. E., and Van Gunsteren, W. F. (2004) A biomolecular force field based on the free enthalpy of hydration and solvation: The GROMOS force-field parameter sets 53A5 and 53A6. *Journal of Computational Chemistry 25*, 1656–1676.

[11] Malde, A. K., Zuo, L., Breeze, M., Stroet, M., Poger, D., Nair, P. C., Oostenbrink, C., and Mark, A. E. (2011) An Automated Force Field Topology Builder (ATB) and Repository: Version 1.0. *Journal of Chemical Theory and Computation 7*, 4026–4037.

[12] Canzar, S., El-Kebir, M., Pool, R., Elbassioni, K., Malde, A. K., Mark, A. E., Geerke, D. P., Stougie, L., and Klau, G. W. (2013) Charge Group Partitioning in Biomolecular Simulation. *Journal of Computational Biology 20*, 188–198.

[13] Koziara, K. B., Stroet, M., Malde, A. K., and Mark, A. E. (2014) Testing and validation of the Automated Topology Builder (ATB) version 2.0: prediction of hydration free enthalpies. *Journal of Computer-Aided Molecular Design 28*, 221–233.

[14] Minoia, A. Buildcstruct, version 1.1. 2011; http://chembytes.wikidot.com/buildcstruct.

[15] Girifalco, L. A., Hodak, M., and Lee, R. S. (2000) Carbon nanotubes, buckyballs, ropes, and a universal graphitic potential. *Physical Review B 62*, 13104–13110.

[16] Strano, M. S., Moore, V. C., Miller, M. K., Allen, M. J., Haroz, E. H., Kittrell, C., Hauge, R. H., and Smalley, R. E. (2003) The role of surfactant adsorption during ultrasonication in the dispersion of single-walled carbon nanotubes. *Journal of Nanoscience and Nanotechnology 3*, 81–86.

Chapter 4

Towards High-Throughput Computational Screening of Carbon Nanotube Solvents

4.1 Copyright Statement

4.2 Introduction

In the previous chapter we successfully demonstrated the efficacy of the corresponding distance method. In this chapter we make use of the method to study ten solvents, selected to cover the entire scale from complete non-solvents, to the best of the solvents available from the large pool that have been previously experimentally tested by Bergin *et al.* [1]. Such a study would previously have been time consuming and difficult, but with the efficiency and speed of the CDM we are able to do it with a fraction of the resources and time.

Bergin *et al.* [1] identified one particularly interesting solvent: N-cyclohexyl-2-pyrrolidone (CHP). CHP was remarkable for performing a factor of five better than even the next best solvent (1,3-dimethyl-3,4,5,6-tetrahydro-2-pyrimidinone, DMPU) with a high yield of around 30%. We discussed in Chapter 3 the use of the Hansen solubility parameters as a predictor for CNT solvents. This was partly successful but includes many false-positive predictions, and it is difficult to spot any trend between these and the ranking of the tested solvents;

in particular they couldn't explain why CHP performed so much better than the rest. We hope that by analysis of PMFs from a broad range of solvents, and analysis of the structure-function relationship and the differences between them, we may be able to discover key features of CHP and its CNT dispersive power.

Having one solvent which performs so superior suggests there is scope still for significant improvements to be made.

4.3 Methods

The corresponding distances method demonstrated in Chapter 3 was applied here with some changes. The tube crossing angle was reduced to 5° to improve resolution and accuracy, particularly important around steep parts of the PMF such as the ttPMF minimum. The Lennard-Jones cut-off radius was increased to 1.6nm, again, for improved accuracy.

An improved routine to integrate the mean force, $F(x)$, was developed to remove high frequency oscillations that are as a result of the four branches of carbon nanotube in the system, and the alternating structure of the tubes themselves. These four branches of tube (Figure 4.1) are not necessarily identical depending on the pivot point of the tubes. Additionally, the tubes have a repeat unit containing two *"rings"* of carbon atoms with different atomic positions around the tubes, and each set of alternating rings can have very different contributions to the mean force (Figure 4.2). The four branches and two ring types give 8 different (very smooth) force curves which we first integrate separately, before averaging the four branch contributions by local interpolation of each ring type and then summing these two contributions to obtain the PMF.

FIGURE 4.1: The four branches in a CDM simulation. Depending on exactly where crossing point is the four branches may not be identical.

A summary of the simulation parameters used can be found in Table A.2.

4.4 Results and Discussion

Ten solvents (Figure 4.3) were selected from the experimental study by Bergin *et al.* [1]. They were selected to cover the full spectrum of solvents and non-solvents. For obvious reasons,

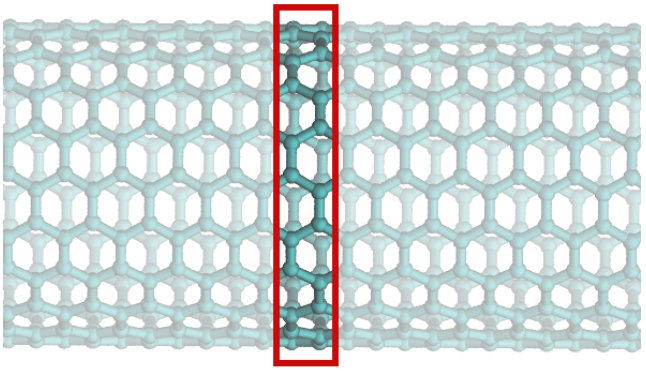

FIGURE 4.2: A 10,10 nanotube highlighting one unit cell. There are two rings of C atoms which are differentiated only by their relative rotation around the cylinder axis.

we included the best of the tested solvents, CHP. We also include $CBrCl_3$ for comparison because of the in-depth study already performed on it in Chapter 3.

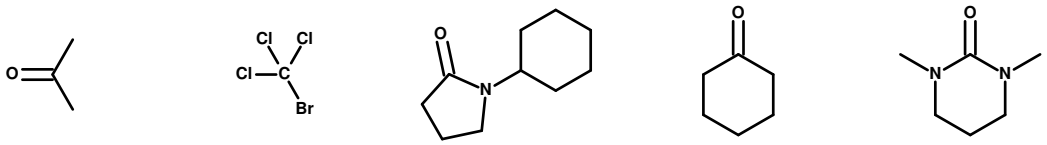

(A) acetone (B) $CBrCl_3$ (C) CHP (D) cyclohexanone (E) DMPU

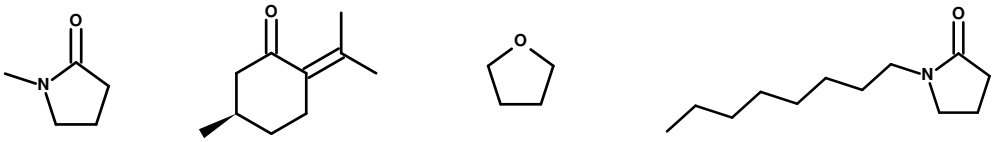

(F) NMP (G) pulegone (H) THF (I) N8P

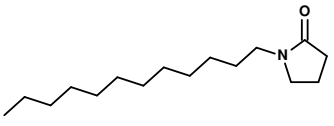

(J) N12P

FIGURE 4.3: The 10 solvents tested. Further information on each can be found in Appendix C.

4.4.1 Comparison of Solvents and Correlation to Experimental Results

We used the CDM to obtain the PMF for a pair of 10,10 nanotubes (the same as those simulated in Chapter 3) for each of the selected solvents (Figure 4.4). Given that we have such a wide variability in performance amongst these solvents it is surprising to find that, at first glance, all the PMFs are quite similar. Certainly, we would at least expect that CHP (performing significantly better than any other solvent), would stand out in some way, but it does not: we will see that seemingly small differences in the PMF are responsible for large differences in solvent performance.

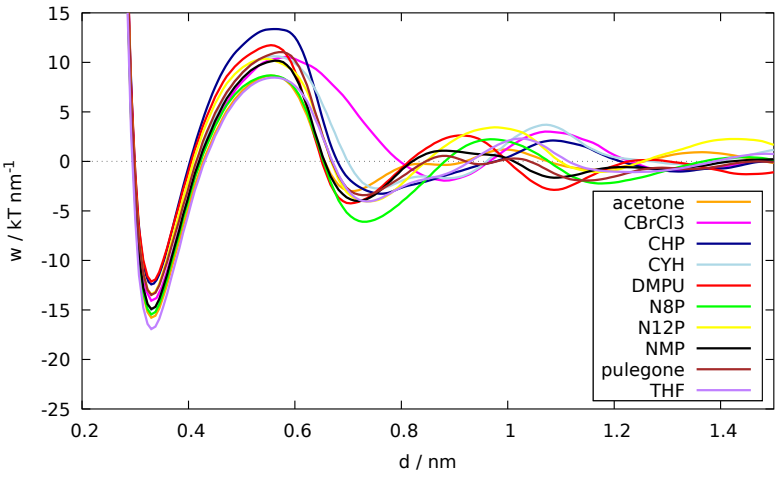

FIGURE 4.4: PMF of CNTs in all simulated solvents. Differences are small but large enough to have a large effect on solvent/dispersant quality (see text).

The single most significant observation from Figure 4.4 is that none of the tested solvents have an aggregate energy, $w_{agg.}$, above zero; none of these "solvents" are solvents in the *thermodynamic* sense. They all destabilise the aggregate significantly ($w_{\text{agg}} = -44\ \ kT\ \text{nm}^{-1}$ for two 10,10 CNTs in a vacuum) but fail to create a thermodynamically stable dispersed state.

If they are not thermodynamic solvents, then logic would dictate that the successful solvents are likely dispersants. In fact, each solvent's PMF shows a re-aggregation barrier, though, as a consequence each solvent also has a dispersion barrier. This would begin to explain why exfoliation of CNTs is so difficult: all of these solvents have large barriers to dispersion ($w_{\text{disp}} = 25\ \ kT\ \text{nm}^{-1}$), far above that which could be activated via thermal fluctuations. The proposed un-zippering mechanism [2] (see the Section 2.7) suggests this kind of exfoliation process requires a continuous input of energy along the entire length of the tube.

Re-examining Figure 4.4 while considering the above, we notice that CHP has the largest re-aggregation barrier, which is consistent with the experimental observation that CHP is the best of the tested solvents. Re-aggregation of colloidal suspensions is a thermally activated

process: if we assume an Arrhenius like behaviour for this process then the lifetime of the dispersion, τ, is linked to the re-aggregation barrier, w_{reagg}, via

$$\tau \propto \frac{1}{k_r} \propto e^{w_{\text{reagg}}/kT} \ , \tag{4.1}$$

where k_r is the rate constant. Assuming a similar pre-exponential factor between different solvents, we can derive an expression for the lifetime ratio of two solvents (A and B).

$$\frac{\tau_A}{\tau_B} \propto e^{(w^A_{\text{reagg}} - w^B_{\text{reagg}})/kT} \tag{4.2}$$

We see that the lifetime ratio between the two solvents is linked to the difference in barrier height by an exponential function: small differences in the barrier height will create large differences in dispersion lifetime. Moreover, the units of the PMF are *kT per nanometre*, so the lifetime ratio increases rapidly with the length of the tube-tube contact. For example, CHP has a re-aggregation barrier of 16.6 kT nm^{-1} and $CBrCl_3$ has a re-aggregation barrier of 12.4 kT nm^{-1}. At 1nm contact length, the lifetime ratio between these two solvents is 81.5. At 5 nm contact length, the lifetime ratio is 3.6×10^9.

This exponential relationship suggests that the calculated dispersion barriers for each solvent molecule, w_{agg}, should be compared with the experimentally measured CNT loading, C_{max} on a logarithmic scale. Figure 4.5a shows a clear link between the two sets of data, with a particularly strong correlation at the top right of the graph, where the best of the solvents are sorted largely in the correct order.

It is also pertinent to check for the correlation between the experimental results and the two other relevant quantities from the PMF: the dispersion barrier (w_{disp}, Figure 4.5b) and the absolute aggregate stability (w_{agg}, Figure 4.5c). In all cases, the barrier to dispersion is large, with no correlation to the experimental data. One might expect an inverse correlation (i.e. a smaller dispersion barrier leads to more dispersed tubes), but in fact it is the best solvent, CHP, that has the largest dispersion barrier. This appears to be a contradiction, but can be explained because the re-aggregation barrier and dispersion barrier are linked by the height of the maximum from the first solvent layer in the PMF (≈ 0.5 nm for all solvents).

The better dispersants tend to be the molecules which the least stable aggregates (closer to being thermodynamic solvents), reinforcing our understanding from Chapter 3 that it is the short range solvent-mediated interactions that are responsible for both effects. However, in

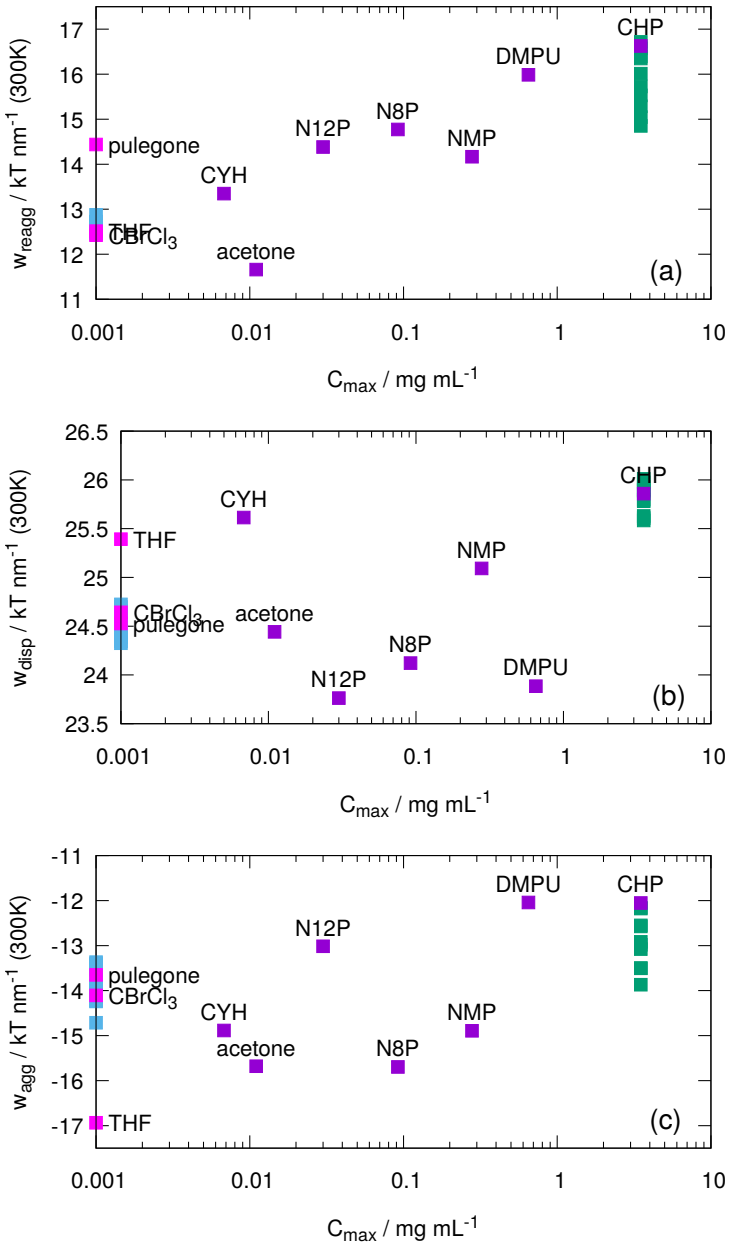

FIGURE 4.5: The reaggregation barrier (a), dispersion barrier (b) and stability of the aggregated state (c) in all solvents against experimentally achieved CNT loading $C_{\max}$ on a log scale, clearly showing the excellent correlation between the reaggregation barrier and the experimental results. Solvents with $C_{\max} = 0$ are indicated with a light purple square and have been placed (artificially) on the vertical axes. The spread of data over 10 simulations for CHP and $CBrCl_3$ are shown in green and blue respectively, with the original data point for each shown in purple.

all cases studied the solvents have a large, negative w_{agg}, so the aggregates in even the best candidate thermodynamic solvents are very stable.

The results suggest that exfoliation in all the experimentally tested systems is achieved via a dispersion mechanism, and none of them are acting as thermodynamic solvents. They also suggest that the dispersion barrier calculated from the CDM is the correct function to assess dispersant quality.

4.4.2 Data Quality

Because the predicted performance of any given solvent is very sensitive to small changes in the reaggregation barrier height, it is important to consider the uncertainty in these data. To do this, 10 repeat runs of two solvents were performed: CHP, which was the best solvent tested and also happens to be one of the largest; and $CBrCl_3$, which was one of the poorest solvents and also one of the smallest.

All ten data points for both solvents are shown alongside the rest of the results in Figure 4.5. The data for CHP and $CBrCl_3$ spread over approximately 2 kT nm^{-1} and 0.5 kT nm^{-1} respectively. The difference in spread is most likely related to the size of the solvent molecules. $CBrCl_3$, as a smaller molecule, has much shorter translational and orientational relaxation times meaning it can sample much more of its phase space than CHP within the time frame of our simulations. Importantly, the uncertainties in these data do not affect the overall trend between the results of the experimental solubility tests and the calculated reaggregation barrier height.

The spread of data for the aggregate stability is around 2 kT nm^{-1} (15%) in both cases; this is good enough to be able to make the distinction between (thermodynamic) solvents and non-solvents.

4.4.3 Structure-Function Relationship

We have so far been able to link the amount of dispersed tubes in experiment to our simulations via the height of the re-aggregation barrier in the PMF. The shape of the PMF is determined by the stability of first layer. This, in turn, is determined by three things: the interactions between the molecules in the first layer and the tube surface; the interactions between the orientationally ordered molecules within the first layer; and the interactions of the first layer with the bulk. These interactions are ultimately dictated by the chemical structure of the solvent. In order to move beyond a trial-and-error approach to CNT solvent

design, we need to understand the link between the chemical structure of a solvent molecule and the resulting PMF.

As the structure-function relationship is complex, we have limited our analysis to a subset of our tested solvents: $CBrCl_3$, DMPU, and CHP. The first performs poorly in both experiment and simulation and the latter two perform well.

In this model the tubes have no electrostatic partial charges so the only forces acting between the solvent and the tubes are van der Waals forces, modelled here by a 6-12 Lennard-Jones (LJ) potential. A few relevant examples are shown in Figure 4.6.

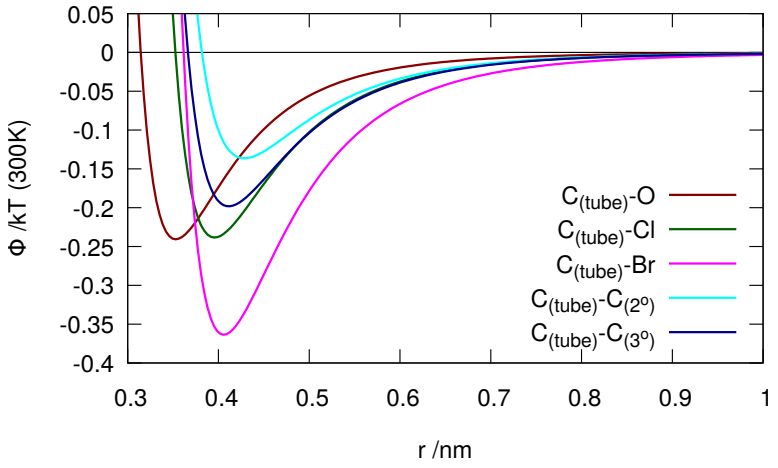

FIGURE 4.6: Lennard-Jones potentials for the interaction of CNT carbon atoms with different solvent atom types. The used unified-atom forcefield integrates bonded hydrogen atoms into the carbon atom which creates different potentials for each possible number of bonded H atoms, indicated by 2° for two hydrogen atoms, for example. It should be noted that although the depth of the attractive potential well varies by more than a factor of two across the different atoms, its position shifts by less than 0.1nm.

The actual structure of the solvent as two tubes approach each other is quite difficult to analyse. We saw in Chapter 3 that the confined, stable single layer (i.e. where $F(d) = 0$) has a structure that is very similar to that around a single, isolated tube and this is much easier to analyse.

The radial density profiles in Figure 4.7a describe layering present at an atomic level within the first and second layers of solvent molecules. The dominant feature of each radial density profile in Figure 4.7a is a large density peak common to each solvent molecule at $R \approx 0.38$ nm (where R is the distance from the tube surface) indicating a dense layer of atoms at the surface of the tube.

R here corresponds to approximately $\frac{1}{2}d$ in the PMF (Figure 4.4); there is one R between the first tube and the solvent layer, and a second R from the solvent layer to the second tube. The first later density peak ($R = 0.38$ nm) maps to approximately $d = 0.76$ nm, which

is where the large repulsive peak in the PMF begins, demonstrating that it is the first layer responsible for generating most of the solvent mediated forces on the tubes.

The position of the first peak is similar for each solvent because it depends only on the van der Waals radius of the closest atoms, which is fairly similar across all the solvents. The solvent atoms can also move into the holes in the hexagonal carbon structure of the tube, further reducing the influence of the atom's size.

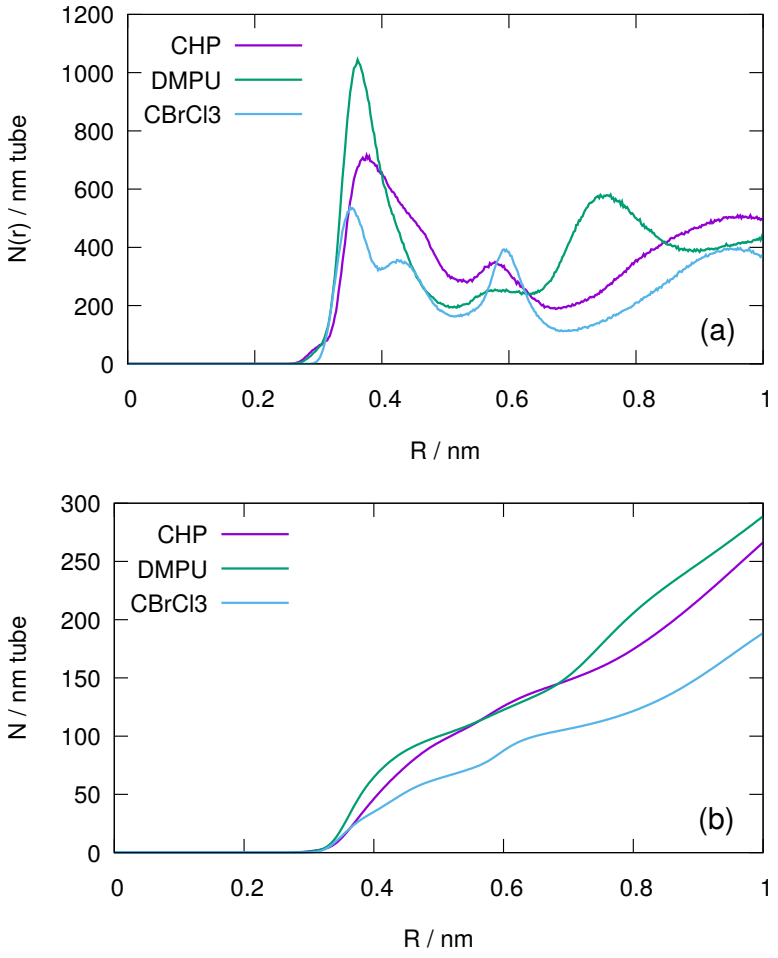

FIGURE 4.7: (a) The number of solvent atoms as a function of distance from the tube surface R and (b) the accumulated number of solvent atoms from the tube surface. Alkyl hydrogen atoms are not included as they are implicit in this unified atom forcefield.

After the first layer it is the orientational order of the adsorbed molecules that determines their density profile. This is driven by the different interaction energies of the solvent atoms with tube, and their position with the solvent molecule.

The structure of $CBrCl_3$ around CNTs has been extensively analysed previously (Chapter 3). To recap: $CBrCl_3$ is a tetrahedral molecule but with its high symmetry broken by the presence of a bromine atom. The most stable configuration of this molecule sees the bromine atom located preferentially at the tube surface (due to the stronger $C_{tube} - Br$ potential)

alongside two chlorine atoms, while the third chlorine atom points straight out from the tube (Figure 4.8iii).

The three directly adsorbed halogens are responsible for the density peak at $R \approx 0.38$ nm, the solvent carbon atom at the centre causes the shoulder on the right of this peak, and the remaining halogen atom causes the smaller peak at $R \approx 0.6$ nm (Figure 4.7a). Beyond $R \approx 0.7$ nm is the structure of the second solvent layer.

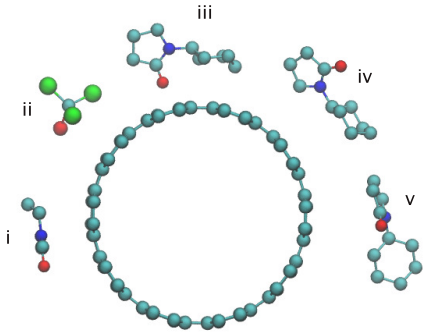

FIGURE 4.8: Configurations of: (i) DMPU, (ii) $CBrCl_3$ and (iii - v) CHP around a nanotube. Alkyl hydrogen atoms are not included as they are implicit in this unified atom forcefield.

The chlorine atom pointing out from the tube surface gives the repulsive region of the smPMF (magenta line in Figure 4.9) a distinctive long range (c.f. the other solvents between $d = 0.6$ nm and $d = 0.8$ nm in Figure 4.4).

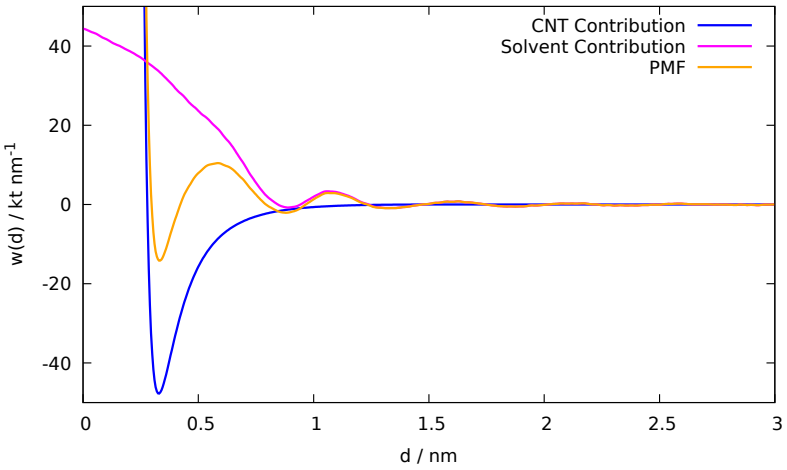

FIGURE 4.9: The PMF curves for a pair of 10,10 CNTs in $CBrCl_3$, including the tube/tube part (ttPMF, blue), the solvent mediated contribution (smPMF, magenta) and the full PMF (yellow).

From large d, as the tube/tube distance is decreased, the layers of $CBrCl_3$ molecules are compressed and forced to re-orientate before being squeezed out layer by layer, creating the

oscillations in the PMF found beyond $d \approx 0.8$ nm. The large repulsive peak in the smPMF at small d is caused by the squeezing out of the last layer: the inner-most layer interacts much more strongly, and specifically with the tubes than the others so results in a much larger force.

From the position of the first peak in the radial densities we can conclude that the last solvent atom has left the gap between the tubes just before the peak of the PMF is reached from the right. The above all occurs at tube/tube distances beyond the minimum of the ttPMF. Because the ttPMF is relatively small in this region, when the ttPMF and smPMF are summed, the PMF in this region is dominated by the contribution from the smPMF resulting in the peak that creates the reaggregation barrier.

Further increases in the smPMF at even smaller d, driven by solvent desorption from increased confinement, do not contribute to the reaggregation barrier as the ttPMF becomes very steep and dominates the PMF. This increase does, though, contribute to the destabilisation of the aggregated state.

We see that good adhesion of the first layer of solvent is critical both for a good dispersant and a good thermodynamic solvent. The strength of this adhesion is determined by the number density of atoms in the first layer and the strength of each atom's interaction with the tubes. The interactions are strongest at close range, so it is the atoms at the surface of the tubes which contribute most.

In $CBrCl_3$, the resultant smPMF is not quite large enough to compensate the large ttPMF minimum sufficiently to create an effective dispersion barrier. This is most likely due to the relatively low density of atoms at the surface of the tubes (Figure 4.7a) owing to the large van der Waals radius of the halogen atoms and long carbon-halogen bond lengths preventing more efficient packing.

DMPU is one of the best performing dispersants and has the highest first peak in the radial atom densities in Figure 4.7a. It sits essentially flat on the tube surface (Figure 4.8i) which disadvantages the molecules somewhat as there is no additional stabilisation from atoms that are further from the surface.

CHP, the best of the dispersants, has a lower atom density at the surface but has additional longer ranged atoms owing to CHP's extended structure; it shows a second maximum similar in magnitude to that of $CBrCl_3$. CHP can adsorb with either one of its rings flat on the tube surface, but the second ring remains perpendicular to this and sticks out, leading to the three configurations in Figure 4.8iii-v.

The lower atom density in the first peak for CHP in Figure 4.7a seems to be compensated for by the higher density further away. The total numbers of atoms in the first layer for CHP

and DMPU are very similar but both significantly higher than for $CBrCl_3$ (Figure 4.7b). Given our understanding thus far we would expect that CHP and DMPU would both be better dispersants than $CBrCl_3$, and this is exactly what we have found.

This understanding is a first step towards rational solvent design. However, the problem is enormously complex: while we can take a known dispersant and discern the structural characteristics that make it effective (or not), it is much more difficult to predict solvent performance from just a molecular structure.

4.4.4 The Pulegone Outlier

The notable outlier in Figure 4.5a is pulegone (Figure 4.3g). The simulation suggests that pulegone should have a dispersion stability similar to that of N8P, N12P or NMP. However in the experiment it dispersed no CNTs. Although the experimental results have, to our knowledge, not been confirmed independently, they have been remeasured several times. Thus, the most likely cause of the discrepancy would be a deficiency in the forcefield.

The most obvious difference between pulegone and N8P, N12P or NMP is the absence of a nitrogen atom, i.e., pulegone does not have an amide group. As amide groups carry large dipoles, which are likely to locally polarize the nanotubes, they strengthen specifically the tube/solvent interaction. Such an effect is not captured by standard MD forcefields. It is, therefore, possible that our model and all other standard forcefields underestimate the performance of all amide solvents. Thus, polarizable forcefields should be considered in future work with high priority.

4.5 Conclusion

Here, we have used the corresponding distances method (CDM) to analyse the CNT-dispersion quality of a range of solvents. The high efficiency, resolution and accuracy of the method has allowed us to study many more solvents than previously possible in one study.

Our model predicts that none of the solvents are creating thermodynamically stable solutions. We see that the size of the re-aggregation barrier is highly predictive for the dispersive power of a solvent indicating that these molecules are in fact dispersants.

The excellent correlation with experimental data and the ability of the CDM to simultaneously assess solvent and dispersant power make it an excellent tool to use in further research.

While we have identified above some characteristics of a solvent that are desirable (a high density of solvent atoms in the first solvent layer, for example), the problem still remains

difficult to solve. This is partially because of the difficulty in establishing a malleable link between the solvent structure and the PMF, and partly because chemical space is huge and difficult to effectively search through.

This sort of problem would lend itself well to an automated, computational optimization to screen for potential solvents. The CDM provides the necessary fitness functions in just one simulation, at a speed and accuracy that make this approach feasible with relatively modest computational resources. Chapter 6 will present the first steps towards such a system,

Bibliography

[1] Bergin, S. D., Sun, Z., Rickard, D., Streich, P. V., Hamilton, J. P., and Coleman, J. N. (2009) Multicomponent Solubility Parameters for Single-Walled Carbon Nanotube-Solvent Mixtures. *ACS Nano 3*, 2340–2350.

[2] Strano, M. S., Moore, V. C., Miller, M. K., Allen, M. J., Haroz, E. H., Kittrell, C., Hauge, R. H., and Smalley, R. E. (2003) The role of surfactant adsorption during ultrasonication in the dispersion of single-walled carbon nanotubes. *Journal of Nanoscience and Nanotechnology 3*, 81–86.

Chapter 5

Design Rules for Graphene Solvents and Dispersants Derived Using the Corresponding Distances Method

5.1 Copyright Statement

5.2 Introduction

So far we have focused just on a one dimensional material (carbon nanotubes). The CDM in principle will also work with two dimensional materials, and here we will test it on graphene.

Graphene is structurally very similar to carbon nanotubes (graphene is essentially a rolled out CNT), and also has very promising physical properties. First isolated in 2004, it has attracted great interest and investment. Graphene was the subject of the 2010 Nobel Prize in Physics [1]. Applications include printable electronics [2], electrodes for energy storage and sensors [3], laminated membranes for water purification [4, 5] or the production of enhanced composite polymeric materials [6, 7].

Graphene (again, as carbon nanotubes) suffers from poor yields and overall loadings with poor rates of true individualisation, which present barriers to widespread and cheap industrial usage.

The same group who conducted the carbon nanotube experiments, which we used as the basis of our comparisons in Chapters 3 and 4, also conducted a similar study on graphene [8], once again correlating the results to solubility parameters and solvent surface tension with the aim of creating a set of predictive parameters. The result was similar: many poor solvents could be eliminated, but this system was less good at predicting good solvents.

While graphene and CNTs share many similarities, two of the better CNT dispersants, N-methyl-pyrrolidone (NMP) and dimethylformamide (DMF) are ineffective graphene dispersants [9]. Chemically, the two materials are very similar, and this suggests that it is the material geometry that is selecting for these solvents.

We will validate the CDM with graphene and then compare two solvents: $CBrCl_3$ and water. It will also be instructive to compare the PMFs obtained from these two solvents in graphene and CNTs, and whether either of them perform significantly differently. Through these comparisons, our aim will be to create some generalised design rules to inform further work in this area.

5.3 Methods

The corresponding distance method was used as in Chapter 4. The only change required to translate the method from a 1-D to 2-D material was to reduce the crossing angle from 5° to 2°. Reducing the crossing angle improves the approximations of the CDM and we were able to produce accurate PMFs for graphene (Section 5.4).

The water model was SPC/E constrained using SHAKE/SETTLE. [10]. A summary of the simulation parameters used can be found in Table A.3.

5.4 Results and Discussion

5.4.1 Validating the CDM

To test the CDM we employed the same strategy as in Chapter 3; validating against a set of parallel sheet simulations. We again opted $CBrCl_3$ as our test case, simply because we have the best understanding of this molecule of all we have looked at so far. When comparing against the mean forces we obtain almost perfect agreement between the two methods (Figure 5.1a).

The smPMFs (Figure 5.1b) produced by the two methods deviate slightly at small d. This is the same phenomenon we saw when first testing the method against CNTs (Figure 3.6). The

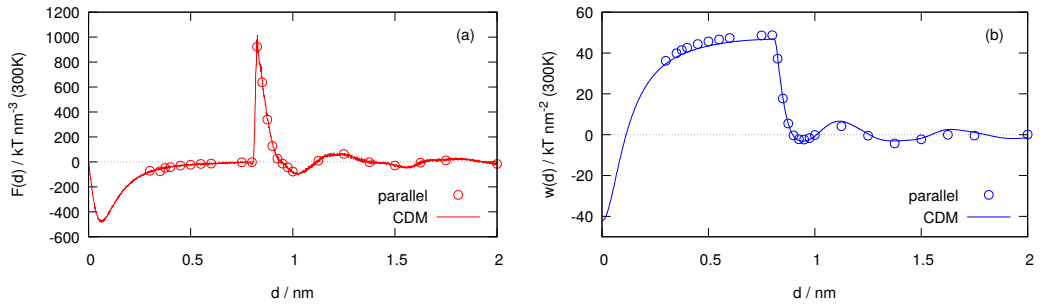

FIGURE 5.1: (a) The sm mean force between a pair of parallel graphene sheets immersed in $CBrCl_3$ to demonstrate the excellent agreement between results from the CDM (solid curve) and the parallel sheet simulations of the system (symbols). (b) The sm potential of mean force obtained from the mean force via integration. The slight disagreement between the two methods is introduced by integration of the sparse data from direct simulation. Parallel sheet data were obtained from Ref. [11].

cause is also the same: the sparse data points of the parallel simulations produce inaccuracies when they are numerically integrated. The PMFs from the CDM here have 4200 data points compared to just 25 from the parallel-sheet simulations.

5.4.2 $CBrCl_3$ and Water

The PMFs of graphene shees in $CBrCl_3$ and in water (Figure 5.2) show intense oscillations, characteristic of the strong layering of the adsorbed solvent molecules. The water smPMF is small in magnitude and short ranged. The repulsive peak of the smPMF is completely dominated by the sheet-sheet PMF (ssPMF) in the PMF and the re-aggregation barrier is small, 11 $kTnm^{-2}$. In contrast, the $CBrCl_3$ smPMF has a large repulsive peak that, crucially, is at its maximum where the ssPMF is still very small. The result is a combined PMF that has a very large re-aggregation barrier of around 40 $kTnm^{-2}$. Neither of these molecules is a thermodynamic solvent for graphene, nor is water a dispersant, but $CBrCl_3$ has a re-aggregation barrier large enough that could make it an effective dispersant.

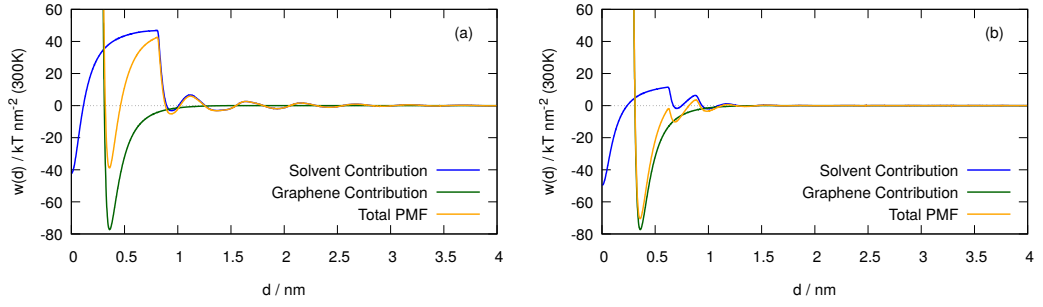

FIGURE 5.2: (a) The $CBrCl_3$ solvent mediated PMF (blue), the direct graphene/graphene interaction potential (green) and the sum of the two, i.e. the full PMF (yellow). (b) as previous, for water. These are PMFs for an infinite graphene sheet.

We know that the orientational structure of the solvent in the first layer is crucial to solvent performance for carbon nanotubes, so we expect this to also have a significant role for graphene. We see from the density profiles in Figure 5.3a that $CBrCl_3$ adopts a very similar orientation on the sheets as it does in CNTs: the bromine atom is predominately turned towards the tube surface, alongside two chlorine atoms, with the third chlorine atom extending straight out from the surface. The second and subsequent layers are much less structured but nevertheless well defined all the way out to $d = 3$ nm and beyond.

In contrast, water has a very simple structure (Figure 5.3b), forming layers just a single atom thick. The oxygen and hydrogen atoms in the first and second layers sit in the same plane and will form a hydrogen bonding network across the surface of the graphene sheet. The first layer is very well defined, the second less so but then subsequent layers are very difficult to see.

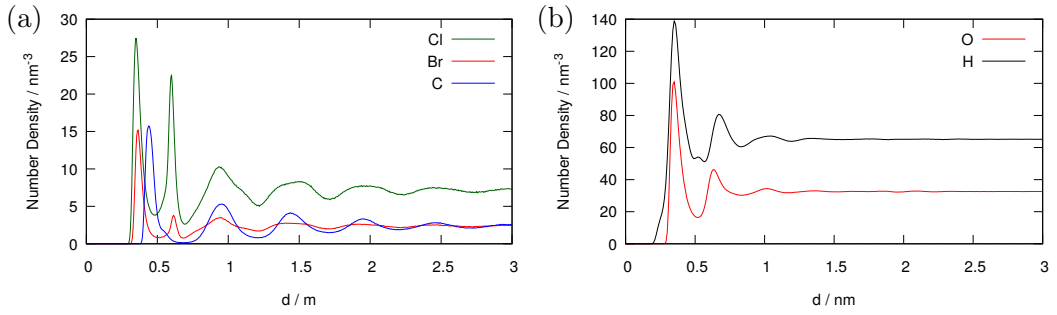

FIGURE 5.3: (a) Density profiles of chlorine, bromine and carbon atoms of $CBrCl_3$ solvent surrounding a single graphene sheet. Molecules in the surface layer are well ordered; most of them adhere to the graphene sheet with the Br and two Cl atoms or with only the Br atom while the three Cl atoms point away from it. The surface layer is quite thick, terminating 0.7 nm away from the sheet.(b) Density profiles of oxygen and hydrogen atoms for a single graphene sheet immersed in water. The first layer is very thin and most hydrogen atoms are located in the oxygen plane as a result of large electrostatic O/H interactions. Note that the hydrogen atoms do not interact with the carbon atoms.

The $CBrCl_3$ first layer is ≈ 0.45 nm wide, the water monolayer is much narrower at ≈ 0.25 nm. Both solvent layers begin ≈ 0.25 nm from the tube surface, due to the similarities in the van der Waals radius of all the atoms (Figure 5.4). Then accounting for the distance to the second sheet, a single water layer is stabilised in pores of $d \approx 0.75$ nm and $CBrCl_3$ is stabilised at $d \approx 0.95$ nm. The thickness of these monolayers corresponds to the location of the first repulsive peak in the smPMF; because the $CBrCl_3$ monolayer is wider, it is squeezed out at larger d than water and the smPMF extends further, interacting where the ttPMF is small, creating the large re-aggregation barrier in the $CBrCl_3$ PMF.

The number density of water ($99.7\ nm^{-1}$) is around three times of that of $CBrCl_3$ ($33.2\ nm^{-1}$), but only the oxygen atom of water interacts with the sheets so they have, approximately equal interaction centre density. Analysis of the van der Waals (Lennard-Jones) potentials

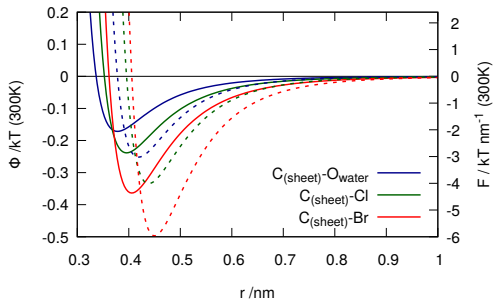

FIGURE 5.4: The van der Waals interaction potentials (solid lines) and the associated force curves (dashed lines) for oxygen/carbon (blue), chlorine/carbon (green) and bromine/carbon (red) pairs, to highlight that to the left of the potential minimum the force is already repulsive, whereas the potential is still negative. Note that the bromine/carbon potential is 50% deeper compared to the chlorine/carbon potential.

(Figure 5.4) reveals oxygen interacts more poorly than both bromine and chlorine, which contrasts with the particularly strong water-water interactions from intermolecular hydrogen bonds. Water interacts much better with itself and worse with the tubes than $CBrCl_3$, so when the final water layer is squeezed out by two sheets there is little (solvent-mediated) energy penalty to pay.

5.4.3 Comparing Graphene and Carbon Nanotubes

The PMFs of $CBrCl_3$ in carbon nanotubes and graphene shown in Figure 5.5 are very different; the graphene smPMF (Figure 5.5a) rises much steeper and the graphene PMF (Figure 5.5b) has a large reaggregation barrier of 40 ktnm^{-2} which is much smaller in CNTs, only 11 kT nm^{-2}. It was established in Chapter 3 that $CBrCl_3$ is a poor dispersant in experiment for CNTs, but the significant re-aggregation barrier present in simulation with graphene suggests it may be an effective dispersant for this material.

Both NMP and DMF are effective CNT dispersants but have been shown ineffective for graphene [9]. We observed in Chapter 4 that while $CBrCl_3$ had a wider layer than NMP, NMP was able to out-perform $CBrCl_3$ owing to a larger interaction-centre density at the tube surface. While strong interactions with the sheets are also critical for an effective graphene dispersant, it appears that more weight should be given to the size and shape of the molecule.

The difference is caused by nano-material shape. The cylindrical geometry of the carbon nanotubes allows the solvent first layer to be removed gradually. As the tubes approach the solvent molecules rotate and the layer re-organises and moves out until eventually the tubes come together. In graphene, this process is much more rapid, and a wide, rigid molecule will effectively resist the graphene sheets approaching at a distance (d) where the ssPMF

is small, when it would rotate out of the way of two approaching tubes, at a much smaller energy cost.

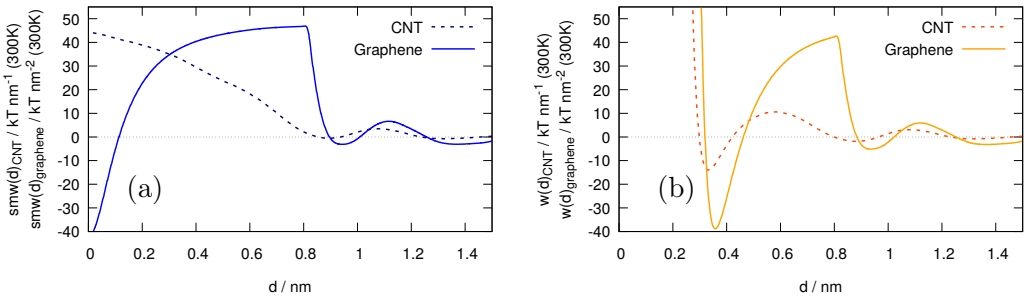

FIGURE 5.5: Comparison of the smPMF (a) and the PMF (b) for graphene (solid) and (10,10) carbon nanotubes (dashed) immersed in $CBrCl_3$ to demonstrate that the geometry of the immersed nano-material has a large effect on solvent performance.

We see in Figure 5.6 that water performs very poorly as either a solvent or dispersant in both materials. The smPMF in both cases is small, short ranged (due to the thin adsorbed layer) and therefore completely dominated by the nano-material particle-particle PMF. The CNT smPMF is marginally larger than that of the graphene smPMF which may be related to the ability of water to form a hydrogen bonding network network around a nanotube [12], which has not been observed in graphene.

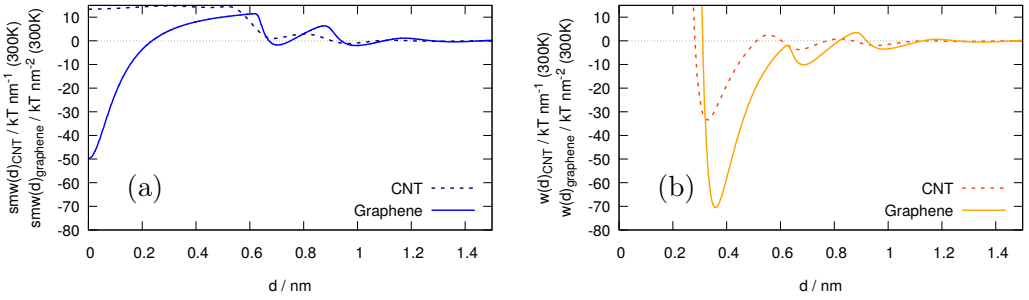

FIGURE 5.6: Comparison of the smPMF (a) and the PMF (b) for graphene (solid) and (10,10) carbon nanotubes (dashed) immersed in water.

5.5 Conclusion

We have used MD simulations combined with the corresponding distances method (CDM) to enhance understanding of the molecular characteristics that make a liquid a good solvent or dispersant for graphene. This is the first time that the CDM has been applied to 2-D materials and our results demonstrate its excellent performance.

We investigated two very different liquids, trichlorobromomethane ($CBrCl_3$) and water to compare their solvent behaviour and, in to understand their difference in performance between graphene and single-wall carbon nanotubes (CNT). As water is a relatively small molecule with very strong intermolecular interactions and comparatively weak adhesion to graphene, it is neither a solvent nor a dispersant for graphene, consistent with our expectations. Nevertheless, $CBrCl_3$ is indicated to be a good dispersant for graphene, but not for CNTs.

Experimental solubility tests have found that CNTs can not be dispersed in trichlorobromomethane [13]. However, here we show that the different geometry of graphene compared to carbon nanotubes can change the potency of a molecule as nano-particle solvent or dispersant. Thus, contrary to the CNT case, our results suggest that $CBrCl_3$ should be a good dispersant for graphene.

Our analysis of the causal chain between structure and function allows us to draw some general conclusions for solvent design. It is plausible that the adsorption free energy, via the stability of the confined monolayer, controls the strength of the repulsive region in the smPMF, whereas the size of the molecules controls its range. Thus, good dispersants are relatively large molecules that adhere well and therefore generate a high reaggregation barrier at distances larger than the range of attraction between graphene sheets. Good solvents must adhere very strongly to compensate the very strong sheet/sheet cohesion, but should be as small as possible to not create a too high exfoliation barrier. These simple "design rules" pave the way to more rational solvent design for graphene.

Bibliography

[1] Nobel Media AB, The 2010 Nobel Prize in Physics - Press Release. 2010; https://www.nobelprize.org/nobel_prizes/physics/laureates/2010/press.html.

[2] Torrisi, F., Hasan, T., Wu, W., Sun, Z., Lombardo, A., Kulmala, T. S., Hsieh, G.-W., Jung, S., Bonaccorso, F., Paul, P. J., Chu, D., and Ferrari, A. C. (2012) Inkjet-Printed Graphene Electronics. *ACS Nano 6*, 2992–3006.

[3] Pumera, M. (2009) Electrochemistry of Graphene: New Horizons for Sensing and Energy Storage. *The Chemical Record 9*, 211–223.

[4] Williams, C. D., Dix, J., Troisi, A., and Carbone, P. (2017) Effective Polarization in Pairwise Potentials at the Graphene-Electrolyte Interface. *J. Phys. Chem. Lett. 8*, 703–708, PMID: 28121448.

[5] Abraham, J., Vasu, K. S., Williams, C. D., Gopinadhan, K., Su, Y., Cherian, C. T., Dix, J., Prestat, E., Haigh, S. J., Grigorieva, I. V., Carbone, P., Geim, A. K., and Nair, R. R. (2017) Tunable Sieving of Ions Using Graphene Oxide Membranes. *Nat. Nanotechnol. 12*, 546–550.

[6] Gonciaruk, A., Althumayri, K., Harrison, W. J., Budd, P. M., and Siperstein, F. R. (2015) PIM-1/Graphene Composite: A Combined Experimental and Molecular Simulation Study. *Microporous and Mesoporous Materials 209*, 126–134.

[7] Shin, Y., Prestat, E., Zhou, K.-G., Gorgojo, P., Althumayri, K., Harrison, W., Budd, P. M., Haigh, S. J., and Casiraghi, C. (2016) Synthesis and Characterization of Composite Membranes Made of Graphene and Polymers of Intrinsic Microporosity. *Carbon 102*, 357–366.

[8] Hernandez, Y. et al. (2008) High-yield production of graphene by liquid-phase exfoliation of graphite. *Nature Nanotechnology 3*, 563–568.

[9] Coleman, J. N. (2013) Liquid Exfoliation of Defect-Free Graphene. *Accounts of Chemical Research 46*, 14–22.

[10] Berendsen, H. J. C., Grigera, J. R., and Straatsma, T. P. (1987) The missing term in effective pair potentials. *The Journal of Physical Chemistry 91*, 6269–6271.

[11] Hardy, A., Dix, J., Williams, C. D., Siperstein, F. R., Carbone, P., and Bock, H. Design rules for graphene and carbon-nanotube solvents and dispersants. *Manuscript submitted for publication*

[12] Li, L., Bedrov, D., and Smith, G. D. (2006) Water-Induced Interactions between Carbon Nanoparticles. *The Journal of Physical Chemistry B 110*, 10509–10513, PMID: 16722760.

[13] Bergin, S. D., Sun, Z., Rickard, D., Streich, P. V., Hamilton, J. P., and Coleman, J. N. (2009) Multicomponent Solubility Parameters for Single-Walled Carbon Nanotube-Solvent Mixtures. *ACS Nano 3*, 2340–2350.

Chapter 6

Optimization and Design of Halo-Methane Solvents

6.1 Introduction

Over the previous chapters we have used the CDM to explore several solvent-material systems, derived from real experiments. The structure-function relationship from the solvent to the PMF is very complicated even for simple molecules, so while we have been able to link the PMF of a CNT or graphene sheet in a solvent back to that solvent's molecular structure, trying use this understanding to do the reverse and design an effective solvent is very difficult. At the end of Chapter 4 we concluded that the next best step is to use the CDM as part of an automated computer optimization. In this chapter we will present the first steps towards such an optimization in a CNT system, and the results of some systems tested as a result of what we learn from it.

This chapter will be presented in two parts. In the first part, we aim to perform an optimization to search for a CNT solvent.

Chemical space is huge and searching it for a molecule to perform any specific function is challenging. The first requirement is to identify the function to be used to assess a molecule's suitability. This fitness function could be almost any property: a partition coefficient, a solubility parameter, protein-ligand binding affinity (often used for drug design), or a combination of several properties. We focus primarily on optimizing for a thermodynamic solvent, for which the defining criterion is that the CNT aggregate should be less stable than the dispersed state, *i.e*, $w_{\text{agg}} > 0$.

Such an optimization, while widely used in the fields of materials and drug design, has not been previously attempted for this particular problem, not least because the calculation of the fitness function was so computationally expensive and difficult. Now that we can use the CDM method to reliably obtain accurate PMF curves relatively cheaply, an optimization becomes more feasible.

Another significant part of the challenge is finding a way to traverse chemical space. One could simply extensively search through a fixed library of molecules; this is very inefficient and can be very costly if the fitness function is any more than trivial to calculate [1, 2]. Smarter methods such as genetic algorithms are more efficient but can have difficulty exploring a large areas of chemical space and still require an amount of manual curation [3, 4]. Newer techniques use neural networks to perform searches but these require specific expertise to develop [5].

This is all to say that performing large-scale optimizations is not straight forward. We will significantly simplify the problem by focusing on only one parameter: the strength of the interaction between the tubes and the solvent molecules, leaving everything else unchanged (see Section 6.2 for details). This reduces the problem down to a continuous, 1-dimensional variable, albeit while creating un-physical systems and limiting us to a single structure.

In the second part of this chapter we will take the lessons learned from the above optimization and apply them to systems which, in contrast to the above, are fully consistent with the forcefield and our other work so far. We have shown design of a CNT solvent to be a very difficult prospect because these systems are very complicated and the physical parameters that affect solvent performance are interconnected. We will see that by isolating one of these parameters in the above optimization we learn important information that can inform our design.

6.1.1 Energy Units

Where previously we have presented results in energy units of kT, we now will use kJ mol^{-1}. While kT is a convenient unit when trying understand thermally activated processes, it has no advantage over measuring in kJ mol^{-1} when determining whether something is a thermodynamic solvent (in both cases the requirement is that $w_{\text{agg}} > 0$). kT is also temperature dependent, and so comparing simulations at different temperatures is difficult and this becomes relevant in the second half of this chapter.

6.2 Part I: Optimization of CX_3Y

$CBrCl_3$ is the template molecule for this optimization, and we refer to it as the generic CX_3Y. In our initial optimization we target one specific characteristic of the system: the tube-solvent interaction strength. We do this by directly modifying the 6-12 Lennard Jones cross potential well depth between the tube and some atoms in the solvent. Importantly, we do this without changing the bulk solvent-solvent or tube-tube interactions. This creates a system which is un-physical.

The Lennard Jones (LJ) equation describes the van der Waals potential ($V(r_{ij})$), between two atoms, i and j, at distance r_{ij}

$$V(r)_{ij} = 4\epsilon_{ij}\left[\left(\frac{\sigma_{ij}}{r_{ij}}\right)^{12} - \left(\frac{\sigma_{ij}}{r_{ij}}\right)^{6}\right], \tag{6.1}$$

where ϵ_{ij} is the depth of the potential well and σ_{ij} is distance (in r) at which the inter-atom potential is zero. When i and j are the same atom type then ϵ_{ij} and σ_{ij} are simply the listed values for that atom from the forcefield. When i and j are different then combination rules are applied. In the GROMOS 53a6 forcefield [6], the cross terms are the geometric mean of the two parameters.

$$\sigma_{ij} = (\sigma_i \times \sigma_j)^{\frac{1}{2}} \tag{6.2}$$

and

$$\epsilon_{ij} = (\epsilon_i \times \epsilon_j)^{\frac{1}{2}} \tag{6.3}$$

In the optimization, we directly modify $\epsilon_{\mathrm{X-CNT}}$ (or $\epsilon_{\mathrm{Y-CNT}}$); changing the depth of the potential between one of the solvent atoms and the nanotube atoms (Figure 6.1). The interaction range ($\sigma_{\mathrm{X-CNT}}$) and the LJ parameters of the bulk solvent remain that of $CBrCl_3$. All other forcefield parameters (such as bond lengths or angles) are unchanged.

We refer to these modified systems as *non self consistent* (NSC); the Lennard Jones combination rules are not applied universally across the system.

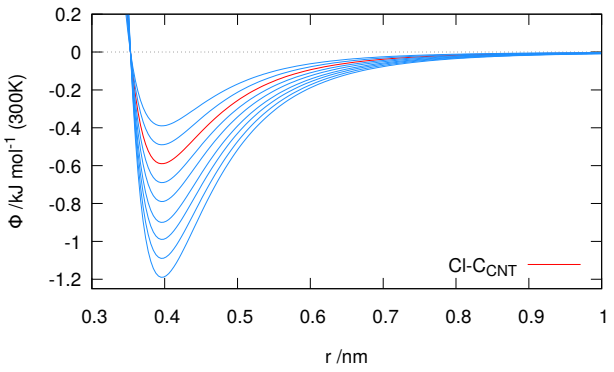

FIGURE 6.1: The red line is the Lennard-Jones cross potential between Cl and a nanotube C atom in the GROMOS 53a6 forcefield. The blue lines are potentials with a modified ϵ_{ij}, used in Figure 6.2

6.2.1 Methods

Because the bulk liquid is unchanged, we can start each simulation from the same well equilibrated starting configuration. This configuration was obtained using the simulation procedure from Chapter 4, except with a change of tube crossing angle (up to 10° from 5°, to reduce simulation times): energy minimization followed by a short isothermal equilibration (0.3ns); isobaric equilibration (1ns); and lastly a second, long isothermal equilibration (10ns) (Table A.4). The starting configuration was created at standard temperature and pressure (300K, 1 bar).

From the pre-equilibrated system, each optimization run then just needs one 10 ns isothermal simulation, of which the first 1 ns is discarded to allow for equilibration following the changes of the tube-solvent LJ parameters. The NSC systems were at 300 K, with constant density across each from the starting configuration.

6.2.2 Results and Discussion

Initially, we modified only $\epsilon_{\mathrm{X-CNT}}$, keeping $\epsilon_{\mathrm{Y-CNT}}$ consistent with a bromine atom in the forcefield at 0.9 kJ mol^{-1} (chlorine). $\epsilon_{\mathrm{X-CNT}}$ is modified from its initial value of 0.9 kJ mol^{-1}.

For this optimization we are most interested in finding thermodynamic solvents, the criterion for this is that the aggregate energy, w_{agg} is greater than zero. In both datasets a solvent is found after sufficiently increasing solvent-CNT attraction (via $\epsilon_{\mathrm{X-CNT}}$, Figure 6.2 or $\epsilon_{\mathrm{Y-CNT}}$, Figure 6.3).

In Figure 6.2 we see that a solvent is found at $\epsilon_{\mathrm{X-CNT}} \gtrsim 0.85$ kJ mol^{-1}. We can fit the data points in Figure 6.2b onto two lines. The change in gradient is caused by a change of orientational configuration of the solvent molecule. At $\epsilon_{\mathrm{X-CNT}} < 0.9$ kJ mol^{-1} (red line), the

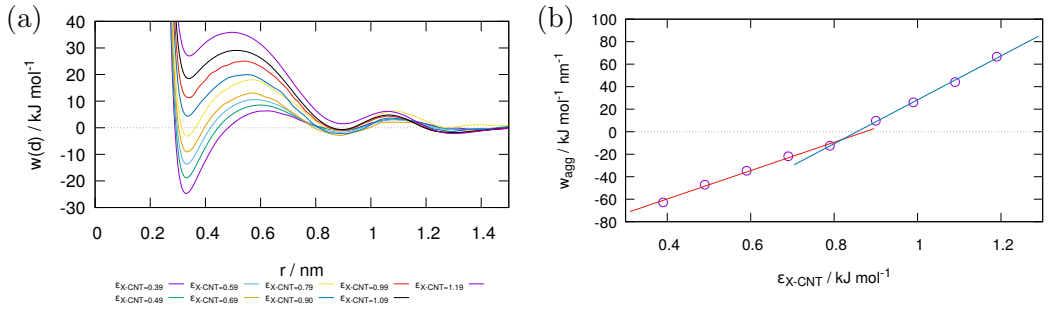

FIGURE 6.2: (a) PMFs and (b) aggregate stability (w_{agg}) as a function of solvent nanotube attraction, of CNTs in CX_3Y for changing ϵ_{X-CNT}.

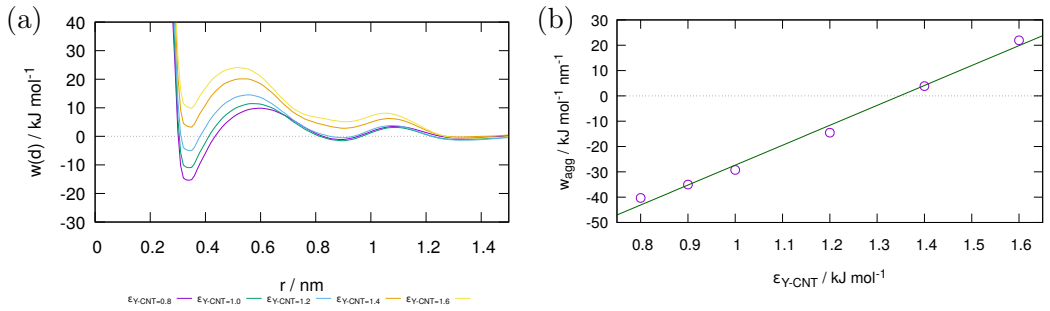

FIGURE 6.3: (a) PMFs and (b) aggregate stability (w_{agg}) as a function of solvent nanotube attraction, of CNTs in CX_3Y for changing ϵ_{Y-CNT}.

Y atom preferentially adsorbs on the tube surface because it has a greater attraction to the CNT atoms (Figure 6.4i). At $\epsilon_{X-CNT} > 0.9$ kJ mol^{-1} (blue line) X is now more attractive to the tubes than Y so the solvent rotates, and all three X atoms are now preferentially adsorbed (Figure 6.4ii). We can see the effect of this in density maps of X atoms around the nanotubes (Figure 6.5).

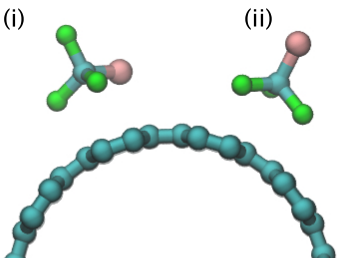

FIGURE 6.4: Orientational configuration of two CX_3Y molecules (X, green and Y, red): (a) where $\epsilon_{X-CNT} > \epsilon_{Y-CNT}$ and (b) where $\epsilon_{X-CNT} < \epsilon_{Y-CNT}$. The molecules rotates so that most attractive atoms are at the surface of the tube.

The red line has a gradient of 126.0 nm^{-1} and the blue line a gradient of 195.0 nm^{-1}: a ratio of 0.65. This almost perfectly correlates to the ratio of preferentially adsorbed X atoms at the surface of the tube in each of these regions (2 : 3).

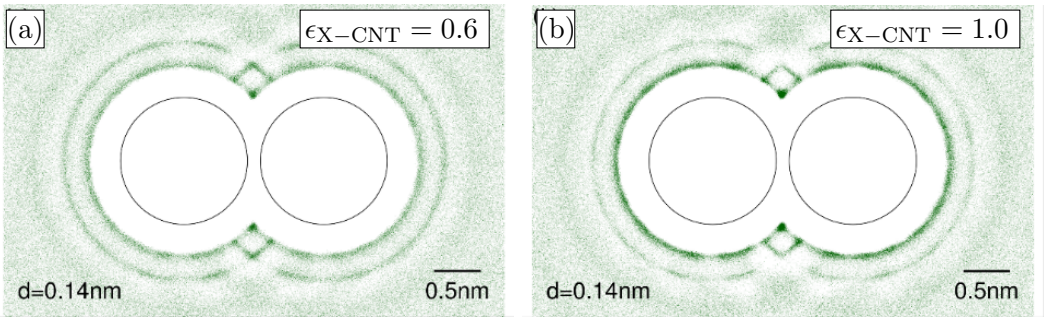

FIGURE 6.5: Density maps of two CX_3Ymolecules: (a) $\epsilon_{X-CNT} = 0.6$ kJ mol^{-1} and (b) $\epsilon_{X-CNT} = 1.0$ kJ mol^{-1}. In (a) the molecule is orientated as in Figure 6.4i. in (b) the molecule has rotated as in Figure 6.4ii and the density map shows a corresponding increase in X density at the tube surface.

We have discussed in previous chapters that there are three main contributions towards the PMF: the strength of the interactions between atoms in the solvent and those of the carbon nanotubes; the orientational configuration of the solvent around the tubes; and a contribution from the bulk solvent which we have so far been unable to define well, but we have assumed to be small compared to the other two factors.

Because we are modifying only the tube-solvent interaction, the bulk solvent remains unchanged and that contribution towards the PMF remains constant. The orientational configuration of the solvent around the tubes also remains constant along each of the two lines in Figure 6.2b. This leaves only the solvent-tube interaction strength to affect the PMF (and the value of w_{agg}) and explains the almost perfect correlation between between the number of adsorbed X atoms and the rate of change of w_{agg} with the change in ϵ_{X-CNT}.

We were also able to create a theoretical solvent manipulating only ϵ_{Y-CNT}(Figure 6.3b), with ϵ_{X-CNT} held at 0.59 kJ mol^{-1} (consistent for a Cl atom in the forcefield). A theoretical solvent is found at $\epsilon_{Y-CNT} \gtrsim 1.38$ kJ mol^{-1}. Again, the data in this range fit well to a straight line.

If we perform a similar analysis of the gradient as above, we find gradient of this line (78.7 nm^{-1}) is slightly too large for the number of atoms whose potentials are being changed (1) and we end up with a ratio of gradients of $1.5 : 2 : 3$ where we expect $1 : 2 : 3$ (Y:$X_{\epsilon_{X-CNT}<0.9}$:$X_{\epsilon_{X-CNT}>0.9}$).

Alongside the potential depth, the other defining characteristic of the Lennard-Jones potential is the length parameter representing the van der Waals diameter of an atom, σ, defined as the distance on the x axis that the potential crosses the y axis at 0 (see Figure 6.1, all the potentials share a common σ of 0.35nm). Recalling that X atoms are based on chlorine and Y atoms on bromine, Y atoms have a larger radius: $\sigma_{X-CNT} = 0.35$ nm, $\sigma_{Y-CNT} = 0.36$ nm (Figure 4.6). The asymmetry caused by the larger radius on the Y atom may push the

X atoms into a steeper part of the LJ potential than they otherwise might, resulting in a different scaling of the effective solvent-tube potential with changing ϵ compared to Y.

We have managed to create several solvents through direct modification of the solvent-tube interaction strength. Ultimately, we must remember that these systems do not directly correspond to anything real; we are manipulating the solvent-tube interactions independently in a way that is completely un-physical. Can we, then, identify analogous *real* molecules for the CX_3Y solvents we have found, and determine how similar they behave in simulation?

6.3 Part II: Design of Halo-Methane Solvents

The first CX_3Y molecule in the above optimization that was found to be a solvent was with $\epsilon_{X-CNT} = 0.9$ kJ mol^{-1} (and Y unchanged). The closest corresponding atom to this is bromine, $\epsilon_{Br-CNT} = 0.9$ kJ mol^{-1}. As the Y atom in CX_3Y is based on bromine, this leads us to CBr_4.

When CBr_4 was simulated it was found not be a solvent. While this initial result is obviously disappointing, it is not a surprise given the other large differences between CX_3Y and CBr_4. In this next section we will identify what these differences are, the effect they have on the PMF and then put what we learn into practice to propose improved solvents.

6.3.1 Methods

The systems following in this section are true to the physics model used in standard molecular dynamics and the GROMOS 53a6 forcefield, to produce results that can relate to real, experimental systems. They were simulated using the same parameters as the non self-consistent, CX_3Y based systems above (Table A.4) with the following steps: energy minimisation, isothermal equilibration, isobaric equilibration and production with simulation times from Table A.5.

6.3.2 Results and Discussion

6.3.2.1 CBr_4

CBr_4 was simulated and found to be a non-solvent: $w_{\text{agg}} = -28.4$ kJ mol^{-1} nm^{-1}, significantly higher than the value found for $CX_{\epsilon_{X-CNT=0.9}Y}$ of $w_{\text{agg}} = 9.7$ kJ mol^{-1} nm^{-1}. There are numerous differences between these simulations. Can we identify those which make the biggest contribution to the decrease of w_{agg}, and tune our solvent system to minimise or

even eliminate them? We will take our CX_3Y solvent and change it one parameter at a time until we obtain CBr_4.

Firstly, the CX_3Y molecule was simulated at 300 K but CBr_4 is solid at this temperature and needed to be simulated at 500 K to liquefy. Changing the temperature of the CX_3Y simulation to 500 K to match reduces w_{agg} to -8.8 kJ mol^{-1} nm^{-1} (shown as the blue arrow/dot in Figure 6.6); it is no longer predicted to be a solvent at this temperature.

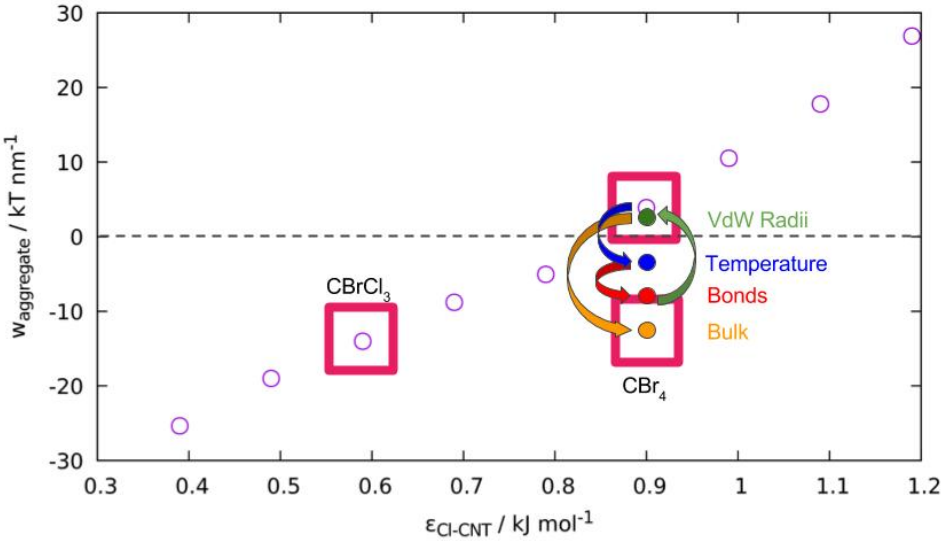

FIGURE 6.6: Purple circles are the same data as Figure 6.2(b). Added to this are solid coloured dots and arrows to demonstrate the change of w_{agg} as we modify parameters of CX_3Y to mutate it step by step into CBr_4 (orange dot).

This could be explained by considering the free energy of solvation, ΔG_{solv}, given by

$$\Delta G_{solv} = \Delta H_{solv} - T\Delta S_{solv} \, . \tag{6.4}$$

where ΔH_{solv} is the enthalpy of solvation, T is temperature and ΔS_{solv} is the entropy of solvation. For any of our CX_3Y solvents ΔH_{solv} could be either positive or negative, we don't know without further investigation, but it is actually not important when we consider the effect of the entropy change.

When the nanotubes are immersed in solvent, the solvent molecules order themselves around the tubes and the total amount of ordering is proportional to the surface area of the tubes. When two CNTs move from the aggregated state to the dispersed state (i.e. they dissolve) the total solvent-accessible surface increases, *increasing* ordering and *decreasing* entropy,

suggesting ΔS_{solv} in a nanotube system is negative. Thus we find that an increasing temperature will make the entropy term in Equation (6.4) more negative, increasing ΔG_{solv} (assuming the direct temperature dependence of ΔH_{solv} and ΔS_{solv} is small over this range) and making the nanotubes less soluble, consistent with our simulations.

We also know that w_{agg} is dependant on the number of adsorbed atoms at the CNT surface (Chapter 4). Increases in temperature drive a decrease in adsorption which will push w_{agg} down and reduce the solubility of the tubes.

The bond lengths between CX_3Y and CBr_4 were corrected next. $CBrCl_3$ is the template molecule for CX_3Y so to correct the bond lengths, the C-X (0.176 nm) bonds were lengthened to that of C-Br (0.189 nm). This further decreased w_{agg} from -8.8 kJ mol^{-1} nm^{-1} to -11.2 kJ mol^{-1} nm^{-1}. Even a small increase (7.3%) in the lengths of 3 out of 4 bonds has a fairly large effect on the aggregate stability.

Similarly, we alter the vdW interaction length parameter between the solvent and the tube, σ_{X-CNT} from 0.347nm to 0.365nm (5.2%). This brings w_{agg} of CX_3Y back above zero to 7.3 kJ mol^{-1} nm^{-1}. The system is now a solvent again, but is further away from CBr_4.

It is clear why the change in potential depth or temperature affects the PMF, but why do changes in seemingly inconsequential length parameters (vdW diameter and bond length) result in such large changes to w_{agg}?

Both the bond length and vdW range parameters affect how the solvent molecule is able to pack on the surface on the nanotube. We previously demonstrated that atom density at the surface is a critical parameter for solvent quality [7] (Chapter 4). Lengthening the X-CNT bond length moves the atoms apart on the surface of the tube, lowering the overall interaction density and reducing w_{agg}.

Counter-intuitively, increasing the vdW diameter of the atoms interacting with the tubes, $\sigma_{\text{X-CNT}}$, increases the number of atoms on the tube surface. Although the atoms are bigger, they are also further away and so the surface area they have to pack on is increased. This results in a net gain of atoms on the surface and w_{agg} is increased.

The last change is to adjust the LJ parameters of the CX_3Y solvent-solvent interactions to be consistent with the forcefield mixing rules and the tube-solvent interactions. Correcting solvent-solvent parameters is the final change between CX_3Y and CBr_4, and w_{agg} of CX_3Y now matches that of CBr_4 (-28.4 kJ mol^{-1} nm^{-1}). The fact this has such a large effect is surprising, it is much more significant than modification of the direct tube-solvent interaction strength. An increase in the solvent-solvent interactions has reduced the quality of the solvent.

It follows that we want a solvent which interacts stronger with the tubes than it does with itself. The LJ cross terms are all coupled to the individual atom parameters (Section 6.2.1), and a single solvent that would behave this way is not easy to find. We could emulate this behaviour with a binary solvent comprising of a weakly interacting (primary) and strongly interacting (secondary) part. Mixtures would also solve the problem of the high temperatures needed for bromo-methane and iodo-methane compounds, because of their high melting points.

6.3.2.2 Mixtures

Results from two binary solvent systems (at 300 K) are presented in Figure 6.7. Each contains a primary solvent which has weak interactions (the *weak* solvent) and a secondary solvent which interacts more strongly (the *strong* solvent). Both systems improve w_{agg} with the addition of the *strong* solvent (measured by percentage of *strong* solvent molecules, $\%\mathrm{N}_{\mathrm{strong}}$, in the system). The *strong* solvent adsorbs preferentially on the nanotube surface, driven by its stronger interaction potential, which in turn causes an increase in w_{agg}.

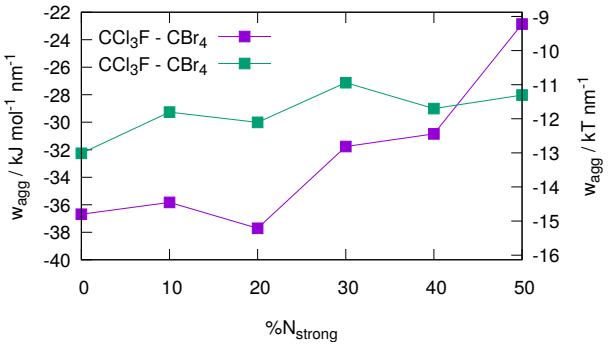

FIGURE 6.7: Aggregate stability, w_{agg}, as a function of the percentage of *strong* solvent molecules, $\%\mathrm{N}_{\mathrm{strong}}$. Units of kT nm^{-1} are given on the right axis for ease of comparison with data from Chapters 3 to 5.

These two systems shared a common *strong* secondary solvent (CBr_4), but differed in *strong* primary solvent. The system with the worst *weak* solvent (CCl_3F, purple line in Figure 6.7) showed the greatest improvement in w_{agg} as $\%\mathrm{N}_{\mathrm{strong}}$ increased, eventually outperforming the other system ($CBrCl_3$, green line in Figure 6.7).

Neither system becomes a thermodynamic solvent ($w_{\mathrm{agg}} > 0$) at up to 50 $\%\mathrm{N}_{\mathrm{strong}}$, although the $CCl_3F - CBr_4$ system achieves the closest result of -23.0 kJ mol^{-1} nm^{-1}. This is a significant improvement on all of the solvents tested in Chapter 4, which ranged between -30.0 and -42.2 kJ mol^{-1} nm^{-1}. Above $\%\mathrm{N}_{\mathrm{strong}} > 50\%$, both systems froze, so this was the upper limit we could explore.

The improvement in w_{agg} from the increase in $\%\text{N}_{\text{strong}}$ in both cases is reasonably clear: a greater proportion of *strong* solvent molecules in the system, means that more are adsorbed on the tube surface at equilibrium, at the expense of the *weak* solvent molecules, driving the PMF up.

While w_{agg} in both systems increases, they increase at different rates, and it is the system with the worst *weak* solvent that improves fastest. In each system, the *strong* solvent interacts less well with the *weak* solvent than it does with the tube, and the *strong* solvent is driven to adsorb on the tube surface. When the interaction potential of the *weak* solvent is lowered, there is a stronger driving force pushing the secondary solvent towards the tube. More precisely, the liquid surface energy around the nanotubes is minimised when the interactions between the liquid and the tube surface are maximised, and this is what causes preferential adsorption of the *strong* solvent molecules.

All else being equal, as in these two systems, with a weaker *weak* solvent, more secondary *strong* solvent is adsorbed and w_{agg} rises faster with increasing $\%\text{N}_{\text{strong}}$.

Although the primary focus is on the aggregate stability, it is also worth considering the behaviour of both the dispersion and the reaggregation barriers. For a thermodynamic solvent we would ideally eliminate all barriers in the system, particularly if we want to avoid the dispersion barrier, w_{disp}, rising as we increase w_{agg}. Even if we find a thermodynamic solvent, a large dispersion barrier would be problematic as increased energy input would be required before the nanotubes could disperse.

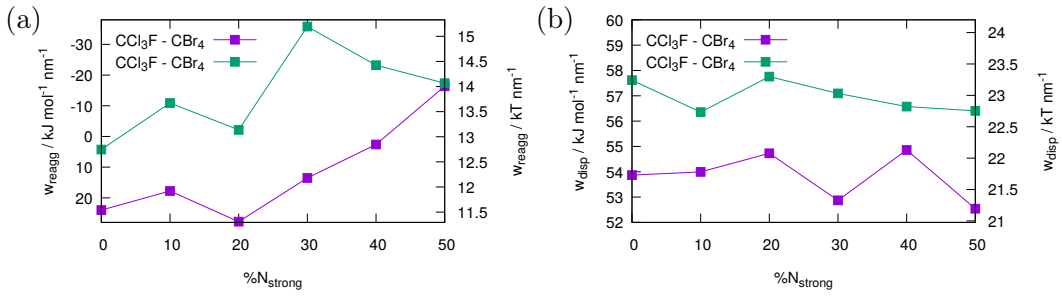

FIGURE 6.8: (a) Dispersion barrier height (w_{disp}) and (b) re-aggregation barrier height (w_{reagg}) as a function of $\%\text{N}_{\text{strong}}$. Units of kT nm^{-1} are given on the right axis for ease of comparison with data from Chapters 3 to 5.

For both solvent systems, the dispersion barrier (Figure 6.8a) fluctuates within approximately ± 2.5 kJ mol^{-1} nm^{-1}($1\ kT$ nm^{-1}) of the pure primary-solvent simulation ($\%\text{N}_{\text{strong}} = 0$). The dispersion barrier is dependent on both the PMF first minimum and first maximum, both of which rise as the smPMF increases, so there is little net change.

The reaggregation barrier, w_{reagg}, rises with $\%N_{strong}$ (as w_{agg} does). This depends on the first maximum and second minimum of the PMF. The first maximum rises with an increasing smPMF but the second minimum changes very little.

At $\%N_{strong} = 0$ neither system would be a dispersant based on the data in Chapter 4. At $\%N_{strong} = 50$ the $CBrCl_3/CBr_4$ system had a reaggregation barrier of 37.8 kJ mol^{-1} nm^{-1} (15.2 kT nm^{-1}), which would rank it third of those solvents tested in Chapter 4. A significant improvement in solvent and dispersant quality has been achieved.

6.4 Conclusion

We have taken advantage of the speed of the corresponding distance method to perform a proof-of-concept optimisation on $CBrCl_3$ in a search for a carbon nanotube solvent. By optimising the the Lennard Jones cross parameters between the solvent halogen atoms and the nanotubes, we were able to obtain thermodynamic CNT solvents.

While the optimized, non-self consistent systems were un-physical, understanding the differences between these un-physical systems and the fully consistent systems led to consideration of solvent mixture systems as a potential route to improved solvents. A mixture of CCl_3F and CBr_4 is the closest to a thermodynamic solvent of all we have tested so far, but there is still significant improvement required.

There are a few ways we could modify these systems further to move towards a thermodynamic solvent. Reducing the interaction strength of the primary solvent has already produced good results, and there is scope for reducing this even further by replacing one or more chlorine(s) in CCl_3F with fluorine. We could also consider increasing the interaction strength of the the secondary-solvent: i.e. using iodine instead of bromine in CBr_4.

There is a large amount of work still to be done to fully explore and understand such mixture systems. Esven before we consider that we not necessarily just limit the search to halo-methane based compounds, the number of permutations of primary solvent, secondary solvent and ratios of each is very large. This, just as in Chapter 4, leads us to the conclusion that the way forward requires a fully automated computer optimization.

Bibliography

[1] Gómez-Bombarelli, R. et al. (2016) Design of efficient molecular organic light-emitting diodes by a high-throughput virtual screening and experimental approach. *Nature Materials 15*.

[2] Hachmann, J., Olivares-Amaya, R., Atahan-Evrenk, S., Amador-Bedolla, C., Sánchez-Carrera, R. S., Gold-Parker, A., Vogt, L., Brockway, A. M., and Aspuru-Guzik, A. (2011) The Harvard Clean Energy Project: Large-Scale Computational Screening and Design of Organic Photovoltaics on the World Community Grid. *The Journal of Physical Chemistry Letters 2*, 2241–2251.

[3] Kanal, I. Y., Owens, S. G., Bechtel, J. S., and Hutchison, G. R. (2013) Efficient Computational Screening of Organic Polymer Photovoltaics. *The Journal of Physical Chemistry Letters 4*, 1613–1623.

[4] O'Boyle, N. M., Campbell, C. M., and Hutchison, G. R. (2011) Computational Design and Selection of Optimal Organic Photovoltaic Materials. *The Journal of Physical Chemistry C 115*, 16200–16210.

[5] Gómez-Bombarelli, R., Duvenaud, D., Hernández-Lobato, J. M., Aguilera-Iparraguirre, J., Hirzel, T. D., Adams, R. P., and Aspuru-Guzik, A. (2016) Automatic chemical design using a data-driven continuous representation of molecules. *arXiv:1610.02415 [physics]* arXiv: 1610.02415.

[6] Oostenbrink, C., Villa, A., Mark, A. E., and Van Gunsteren, W. F. (2004) A biomolecular force field based on the free enthalpy of hydration and solvation: The GROMOS force-field parameter sets 53A5 and 53A6. *Journal of Computational Chemistry 25*, 1656–1676.

[7] Hardy, A., and Bock, H. (2017) Toward High-Throughput Computational Screening of Carbon Nanotube Solvents. *Langmuir 33*, 12267–12275.

Chapter 7

Conclusion

The corresponding distances method has been demonstrated for two low dimensional materials: CNTs and graphene. The CDM is fast, high resolution, and is able to easily maintain thermodynamic consistency across all data points.

We extensively studied CNT solvents. Current CNT solvents were found to be *dispersants*, not *thermodynamic solvents*. Experimentally tested CNT loading is linked to the height of the re-aggregation barrier by an exponential function: even small changes in structure, that have small effects on the PMF, can produce large differences in the stability of a dispersion.

In general, large molecules are likely to create effective dispersants because they interact with the opposing tube at range where the tube-tube potential is small. This, however, is problematic for a solvent as it will create a large dispersion barrier. Beyond these very broad statements, the structure function relationship between a solvent molecule and its dispersive power is extremely complicated. Rational design of a solvent molecule based on understanding these relationships is not feasible. The logical next step is to employ an automated algorithm to search chemical space.

We demonstrated a proof of concept optimization by modifying the strength of the tube-solvent Lennard Jones interaction and we were able to produce a theoretical CNT solvent, resembling CBr_4. Selectively modifying the LJ parameters in this way is entirely un-physical, but from this we learned important lessons that led us to consider solvent mixtures.

The understanding gained from this optimisation led us to develop a system from a non-solvent/non-dispersant (pure $CBrCl_3$) to a binary solvent system which would be an effective dispersant and ranks the closest to being a solvent of all we have tested ($CCl_3F + CBr_4$).

Upon testing graphene we find that the different geometry of materials (compared to carbon nanotubes) produces different results from solvents. $CBrCl_3$ is a non-solvent for CNTs but

is likely effective for graphene. For graphene it seems that extended structure of a solvent is more important than for CNTs. As with carbon nanotubes, the link from structure to experimental dispersion is complicated and future work should focus on optimization in chemical space.

7.1 Future Work

7.1.1 Other Materials

There are numerous other materials that could be studied with benefit from the CDM. Cellulose nanocrystals (derived from cellulose) are an abundant, naturally occurring material with useful chemical, mechanical and optical properties [1]. The CDM could be used to create a inter-particle potential for a coarse grained cellulose nanocrystal forcefield.

There are several variants of carbon nanotube-like and graphene-like materials such boron nitride nanotubes which exhibit a similar aggregation behaviour. Functionalised variants of carbon nanotubes and graphene have been shown to exhibit different solvent preferences depending on the chemistry of the groups present [2]. It is also possible to use solvents to select carbon nanotubes for properties such as radius, chirality or metallic/semi-conducting [3–6]. The large number of simulations that would be required to study this behaviour makes the CDM particularly appropriate.

7.1.2 Polarisable Forcefields

Polarisable forcefields were identified in Chapter 4 as a possible improvement to our model. Carbon nanotubes and graphene are highly polarizable and polar solvents, such as amides, are likely to introduce local charge which is not captured in our current simulations. Some literature suggests that charging of the nanotubes could be significant for CNT dispersion [7–11].

This is a short coming of standard molecular dynamics and though there has been much work in the development of polarizable forcefields, they are less mature and much more expensive to use [12]. Comparisons of polarisable and non-polarisable forcefield with quantum mechanics based methods with carbon nano-material fragments indicate non-polarisable methods may be deficient [13–16].

7.1.3 Computer Optimization

We have been able to identify some very broad trends towards effective solvents for carbon nanotubes and graphene, but our research has struggled to find definitive design rules for these solvents; small differences in solvent structure have large, unpredictable effects on solvent quality.

The optimization procedure followed in Chapter 6 can be considered a prototype to a fully automated optimization. To move to a fully automated system that could find a solvent, we need to vastly increase the scope of the optimisation from small variations on one molecule to exploring a much wider area of chemical space. We must also choose a suitable algorithm (there are many kinds [17–19]) to make the decisions that a human operator has made here. Previously, such an optimization would have been computationally expensive and time consuming, but the efficiency of the CDM makes this feasible.

Bibliography

[1] George, J., and Sabapathi, S. (2015) Cellulose nanocrystals: synthesis, functional properties, and applications. *Nanotechnology, Science and Applications 8*, 45–54.

[2] Kim, D. H., Yun, Y. S., and Jin, H.-J. (2012) Difference of dispersion behavior between graphene oxide and oxidized carbon nanotubes in polar organic solvents. *Current Applied Physics 12*, 637 – 642.

[3] Wang, H., and Bao, Z. (2015) Conjugated polymer sorting of semiconducting carbon nanotubes and their electronic applications. *Nano Today 10*, 737–758.

[4] Joo, Y., Brady, G. J., Shea, M. J., Oviedo, M. B., Kanimozhi, C., Schmitt, S. K., Wong, B. M., Arnold, M. S., and Gopalan, P. (2015) Isolation of Pristine Electronics Grade Semiconducting Carbon Nanotubes by Switching the Rigidity of the Wrapping Polymer Backbone on Demand. *ACS Nano 9*, 10203–10213.

[5] Wang, H., Mei, J., Liu, P., Schmidt, K., Jiménez-Osés, G., Osuna, S., Fang, L., Tassone, C. J., Zoombelt, A. P., Sokolov, A. N., Houk, K. N., Toney, M. F., and Bao, Z. (2013) Scalable and Selective Dispersion of Semiconducting Arc-Discharged Carbon Nanotubes by Dithiafulvalene/Thiophene Copolymers for Thin Film Transistors. *ACS Nano 7*, 2659–2668.

[6] Wang, H., Hsieh, B., Jiménez-Osés, G., Liu, P., Tassone, C. J., Diao, Y., Lei, T., Houk, K. N., and Bao, Z. (2015) Solvent Effects on Polymer Sorting of Carbon Nanotubes with Applications in Printed Electronics. *Small 11*, 126–133.

[7] Paliy, M., Consta, S., and Yang, J. (2014) Interactions between Carbon Nanoparticles in a Droplet of Organic Solvent. *The Journal of Physical Chemistry C 118*, 16074–16086.

[8] Voiry, D., Drummond, C., and Pénicaud, A. (2011) Portrait of carbon nanotube salts as soluble polyelectrolytes. *Soft Matter 7*, 7998–8001.

[9] Fogden, S., Howard, C. A., Heenan, R. K., Skipper, N. T., and Shaffer, M. S. P. (2012) Scalable Method for the Reductive Dissolution, Purification, and Separation of Single-Walled Carbon Nanotubes. *ACS Nano 6*, 54–62.

[10] Pénicaud, A., Poulin, P., Derré, A., Anglaret, E., and Petit, P. (2005) Spontaneous Dissolution of a Single-Wall Carbon Nanotube Salt. *Journal of the American Chemical Society 127*, 8–9.

[11] Howard, C. A., and Skipper, N. T. (2009) Computer Simulations of Fulleride Anions in Metal-Ammonia Solutions. *The Journal of Physical Chemistry B 113*, 3324–3332.

[12] Baker, C. M. (2015) Polarizable force fields for molecular dynamics simulations of biomolecules. *Wiley Interdisciplinary Reviews: Computational Molecular Science 5*, 241–254.

[13] Schyman, P., and Jorgensen, W. L. (2013) Exploring Adsorption of Water and Ions on Carbon Surfaces using a Polarizable Force Field. *The Journal of Physical Chemistry Letters 4*, 468–474.

[14] Gao, J. (1997) Toward a Molecular Orbital Derived Empirical Potential for Liquid Simulations. *The Journal of Physical Chemistry B 101*, 657–663.

[15] Li, H., Chowdhary, J., Huang, L., He, X., MacKerell, A. D., and Roux, B. (2017) Drude Polarizable Force Field for Molecular Dynamics Simulations of Saturated and Unsaturated Zwitterionic Lipids. *Journal of Chemical Theory and Computation 13*, 4535–4552.

[16] Lemkul, J. A., Huang, J., Roux, B., and MacKerell, A. D. (2016) An Empirical Polarizable Force Field Based on the Classical Drude Oscillator Model: Development History and Recent Applications. *Chemical Reviews 116*, 4983–5013.

[17] Kanal, I. Y., Owens, S. G., Bechtel, J. S., and Hutchison, G. R. (2013) Efficient Computational Screening of Organic Polymer Photovoltaics. *The Journal of Physical Chemistry Letters 4*, 1613–1623.

[18] O'Boyle, N. M., Campbell, C. M., and Hutchison, G. R. (2011) Computational Design and Selection of Optimal Organic Photovoltaic Materials. *The Journal of Physical Chemistry C 115*, 16200–16210.

[19] Gómez-Bombarelli, R., Duvenaud, D., Hernández-Lobato, J. M., Aguilera-Iparraguirre, J., Hirzel, T. D., Adams, R. P., and Aspuru-Guzik, A. (2016) Automatic chemical design using a data-driven continuous representation of molecules. *arXiv:1610.02415 [physics]* arXiv: 1610.02415.

Appendix A

Simulation Parameters

A.1 Simulation Parameters for Chapter 3

Simulation parameters for Chapter 3 can be found in Table A.1.

A.2 Simulation Parameters for Chapter 4

Simulation parameters for Chapter 4 can be found in Table A.2

A.3 Simulation Parameters for Chapter 5

Simulation parameters for Chapter 5 can be found in Table A.3. The coordinate system is illustrated in Figure A.1.

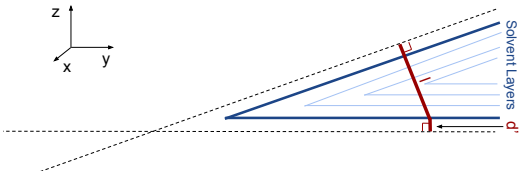

FIGURE A.1: Schematic of the system set up and coordinate system used for the graphene simulations.

A.4 Simulation Parameters for Chapter 6

Simulation parameters for Chapter 6 can be found in Table A.4 and Table A.5.

Production	
Ensemble	NVT
Simulation Time (ns)	10
Timestep (ps)	0.002
Integrator	velocity verlet
VdW and electrostatic cut-off (nm)	1.2
VdW scheme	Lennard Jones 12-6, potential shift
Electrostatic scheme	Reaction Field Zero, potential shift verlet
Thermostat	v-rescale
Thermostat coupling time/constant (ps)	0.1
VdW mixing rule	geometric mean
Integrator	Velocity verlet
Machine precision	double
Neighbour list update frequency (steps)	20
Neighbour list cut-off (ns)	1.5
Isothermal/Isobaric Equilibration	
Ensemble	$NP_z s_{xy} T$
Time (ns)	1
Barostat	berendsen
Barostat coupling constant (ps)	2.0
Compressibility (bar^{-1})	$4{\cdot}10^5$
Isothermal Equilibration	
Ensemble	NVT
Time (ps)	300
Energy Minimisation	
EM Type	conjugate gradient
nsteps	10000
F_{max} ($kJmol^{-1}$)	10^3
Parameters for the energy minimisation and equilibration steps are the same as for the production step unless otherwise stated.	

Table A.1: Simulation Parameters

Production	
Ensemble	NVT
Simulation Time (ns)	10
Timestep (ps)	0.002
Integrator	velocity verlet
VdW and electrostatic cut-off (nm)	1.6
VdW scheme	Lennard Jones 12-6, potential shift
Electrostatic scheme	Reaction Field Zero, potential shift verlet
Thermostat	velocity-rescale
Thermostat coupling time/constant (ps)	0.1
VdW mixing rule	geometric mean
Machine precision	double
Neighbour list update frequency (steps)	20
Neighbour list cut-off (nm)	1.9
Isothermal/Isobaric Equilibration	
Ensemble	$NP_z s_{xy} T$
Simulation Time (ns)	2
Barostat	berendsen
Barostat coupling constant (ps)	2.0
Isothermal Compressibility (bar^{-1})	$4{\cdot}10^5$
Isothermal Equilibration	
Ensemble	NVT
Time (ns)	0.3
Energy Minimization	
EM Type	conjugate gradient
Max. number of steps	10000
F_{max} ($kJmol^{-1}$)	10^3
Parameters for the energy minimization and equilibration steps are the same as for the production step unless otherwise stated.	

TABLE A.2: Simulation Parameters for Chapter 4

Production	
Ensemble	NVT
Simulation time (ns)	10 (water), 21 ($CBrCl_3$), 10 (all CDM)
Averaging (ns)	9 (water), 10 ($CBrCl_3$), 9 (all CDM)
Integrator	velocity verlet
Timestep (ps)	0.002
vdW and electrostatic cut-off (nm)	1.6
vdW scheme	Lennard Jones 12-6, potential shift
Electrostatic scheme	Reaction Field Zero, potential shift verlet
Thermostat	velocity rescale
Thermostat coupling time/constant (ps)	0.1
Neighbour list update frequency (steps)	20
Neighbour list cut-off (nm)	1.9
Isothermal/Isobaric Equilibration	
Ensemble	($NP_{\|\|}s_zT$) parallel-sheet, ($NP_{\|}\_s_xT$) CDM
Simulation time (ns)	1
Barostat	Berendsen
Barostat coupling constant (ps)	2.0
Isothermal Compressibility (bar^{-1})	$4{\cdot}10^{-5}$
Isothermal Equilibration	
Ensemble	NVT
Simulation time (ps)	300
Energy Minimization	
EM Type ($CBrCl_3$)	conjugate gradient
EM Type (water)	steepest decent
Max. Number of steps	10000
Convergence criteria, F_{max} ($kJmol^{-1}$)	10^3
Parameters for the energy minimization and equilibration steps are the same as for the production step unless otherwise stated.	

TABLE A.3: Simulation Parameters for Chapter 5

Isothermal Equilibration/Production	
Ensemble	NVT
Timestep (ps)	0.002
Integrator	velocity verlet
VdW and electrostatic cut-off (nm)	1.6
VdW scheme	Lennard Jones 12-6, potential shift
Electrostatic scheme	Reaction Field Zero, potential shift verlet
Thermostat[1]	velocity-rescale
Thermostat coupling time/constant (ps)	0.1
VdW mixing rule	geometric mean
Machine precision	double
Neighbour list update frequency (steps)	20
Neighbour list cut-off (nm)	1.9
Isobaric Equilibration	
Ensemble (see Section 4.3)	$NP_z s_{xy} T$
Barostat	berendsen
Barostat coupling constant (ps)	2.0
Isothermal Compressibility (bar^{-1})	$4{\cdot}10^5$
Energy Minimization	
EM Type	conjugate gradient
Max. number of steps[2]	10000
F_{max} ($kJmol^{-1}$)	10^3
Parameters for the energy minimization and equilibration steps are the same as for the production step unless otherwise stated.	

TABLE A.4: Simulation Parameters for Chapter 6, Part 1

	t Singular Solvent / ns	t Binary Solvent / ns
Isothermal Equilibration	0.3	0.3
Isobaric Equilibration	1	10
Production	10	20

TABLE A.5: Simulation Time for Chapter 6, Part 2. Simulation parameters remain the same as Table A.4. Binary solvent systems require longer equilibration times to allow the solvent distribution throughout the system to equilibrate.

Appendix B

Force Map Scale-Bars

B.1 Scale Bars

Scales for density maps in Figure B.1 and force maps in Figure B.2 maps are cut-off at each end to provide sufficient contrast in the plot to bring out the important features.

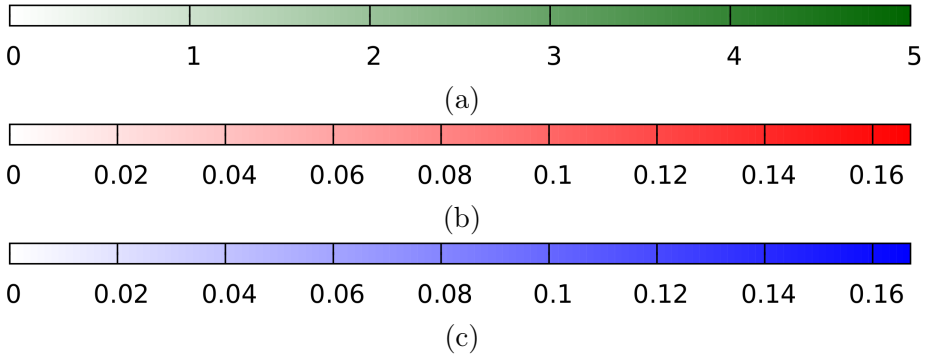

FIGURE B.1: Scale bars for density maps presented in Figures 3.7, 3.10 and 3.12 for Chlorine, a (green), Bromine, b (red), and Carbon, c, (blue) in units of per unit volume, N nm^{-3}.

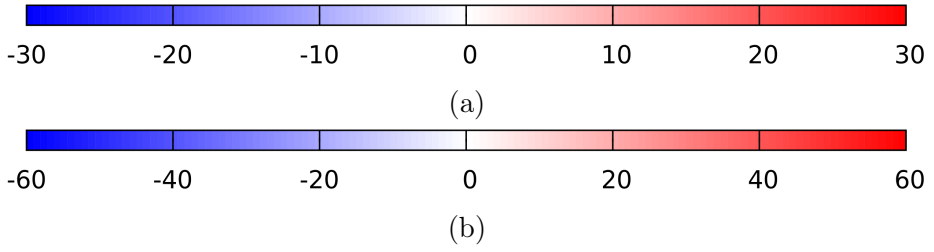

FIGURE B.2: Scale bars for force maps presented in: (a) Figures 3.14 and 3.15, and (b) Figures 3.10 and 3.16. Force densities in (kJ mol^{-1} nm^{-1}) nm^{-3}.

Appendix C

Solvent Data

The 10 solvents used and their full names, structures and SMILES strings are given in Table C.1.

Table C.1: Solvents

Name (abbreviation)	Structure	SMILES
acetone		CC(=O)C
bromotrichloromethane ($CBrCl_3$)		C(Cl)(Cl)(Cl)Br
cyclohexyl pyrrolidine (CHP)	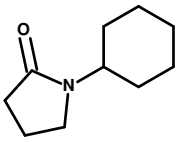	O=C2N(C1CCCCC1)CCC2

Continued on next page

Name (abbreviation)	Structure	SMILES
cyclohexanone	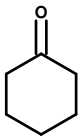	C1CCC(=O)CC1
1,3-dimethyl-3,4,5,6-tetrahydro-2(1H)-pyrimidinone (DMPU)	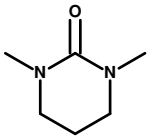	O=C1N(C)CCCN1C
N-methyl-2-pyrrolidone (NMP)	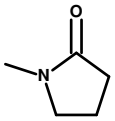	CN1CCCC1=O
N-octyl-2-pyrrolidone (N8P)	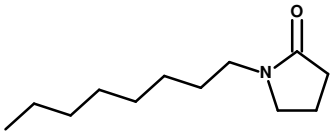	CCCCCCCCN1CCCC1=O
N-dodecyl-2-pyrrolidone (N12P)	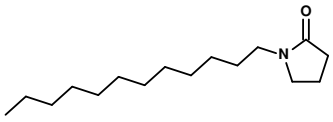	CCCCCCCCCCCCN1CCCC1=O
pulegone	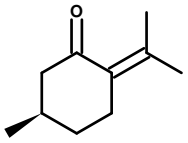	O=C1/C(=C(/C)C)CC[C@@H](C)C1

Continued on next page

Name (abbreviation)	Structure	SMILES
tetrahydrofuran (THF)		C1CCOC1